

# Do we need wavelets in the late Universe?

Luis A. Escamilla,<sup>1,2,\*</sup> Emre Özülker,<sup>3,1,†</sup> Özgür Akarsu,<sup>3,‡</sup> Eleonora Di Valentino,<sup>1,§</sup> and J. A. Vázquez<sup>2,¶</sup>

<sup>1</sup>*School of Mathematics and Statistics, University of Sheffield, Hounsfield Road, Sheffield S3 7RH, United Kingdom*

<sup>2</sup>*Instituto de Ciencias Físicas, Universidad Nacional Autónoma de México, Cuernavaca, Morelos, 62210, México*

<sup>3</sup>*Department of Physics, Istanbul Technical University, Maslak 34469 Istanbul, Türkiye*

We parameterize the Hubble function by adding Hermitian wavelets to the Hubble radius of  $\Lambda$ CDM. This allows us to build Hubble functions that oscillate around  $\Lambda$ CDM at late times without modifying its angular diameter distance to last scattering. We perform parameter inference and model selection procedures on these new Hubble functions at the background level. In our analyses consisting of a wide variety of cosmological observations, we find that baryon acoustic oscillations (BAO) data play a crucial role in determining the constraints on the wavelet parameters. In particular, we focus on the differences between SDSS- and DESI-BAO datasets and find that wavelets provide a better fit to the data when either of the BAO datasets is present. However, DESI-BAO has a preference for the center of the wavelets to be around  $z \sim 0.7$ , while SDSS-BAO prefers higher redshifts of  $z > 1$ . This difference appears to be driven by the discrepancies between these two datasets in their  $D_H/r_d$  measurements at  $z = 0.51$  and  $z \sim 2.3$ . Finally, we also derive the consequences of the wavelets on a dark energy component. We find that the dark energy density oscillates by construction and also attains negative values at large redshifts ( $z \gtrsim 2$ ) as a consequence of the SDSS-BAO data. We conclude that while the early universe and the constraints on the matter density and the Hubble constant remain unchanged, wavelets are favored in the late universe by the BAO data. Specifically, there is a significant improvement at more than  $3\sigma$  in the fit when new DESI-BAO data are included in the analysis.

## I. INTRODUCTION

The standard model of cosmology, the  $\Lambda$  cold dark matter (CDM) model dubbed  $\Lambda$ CDM, provides excellent accuracy in explaining the majority of high-precision cosmological observations despite the simplicity of the model [1–17]. Yet, it faces numerous challenges, both theoretical and statistical. The most prominent of these are the Cosmological Constant Problem [18–20] and the Coincidence Problem [21–23] on the theoretical side, and the  $H_0$  tension [24–35] and the  $S_8$  tension [36–49] on the observational side; see also Refs. [50–52] for reviews of the tensions and anomalies in cosmology.

A plethora of alternative models to  $\Lambda$ CDM have been proposed to provide a better description of the observed universe [53–169] and many studies work on reconstructing the expansion history or relevant cosmological functions from the available cosmological data [170–182]. However, it is still far from clear what it takes for a model to overcome the challenges faced by  $\Lambda$ CDM. Due to the success of the  $\Lambda$ CDM model in accurately explaining most observations, a considerable number of proposed alternatives act as extensions or slight deviations from the standard model. In this way, many of the characteristics contributing to the success of the standard model are preserved. It has recently been shown in Ref. [183]

that, due to the very high precision of the measurement of the angular scale of the sound horizon at last scattering from the cosmic microwave background (CMB) observations by the *Planck* collaboration [8], if an alternative model is to retain the consistency of  $\Lambda$ CDM with this measurement without modifying the comoving size of the sound horizon and the  $H_0$  parameter, the Hubble radius  $H^{-1}(z)$  of the alternative model should deviate from that of the  $\Lambda$ CDM model in the form of *admissible wavelets*, which are localized oscillatory functions with a vanishing integral.

Wavelets can also be conveniently built by differentiating probability density functions, and they provide an arbitrary number of oscillations through differentiation without increasing the number of free parameters. These deviations from  $\Lambda$ CDM at the background level can then be mapped to underlying physics, such as an evolving dark energy (DE) density or time-varying gravitational coupling [183]. In this regard, to gain insight into potential solutions to the inherent problems of the standard model, a wavelet extension of  $\Lambda$ CDM can be characterized using parameter inference techniques such as Markov Chain Monte Carlo (MCMC) or Nested Sampling.

In this paper, we study how a wavelet-extension scenario of the standard model performs compared to  $\Lambda$ CDM when applying parameter-inference and model-selection procedures. The paper is organized as follows: in Section II, we describe the wavelet deviations in the Hubble radius studied in this paper; in Section III, we present the datasets and methodology used; in Section IV, we discuss the results; and in Section V, we conclude with our findings.

\* [luis.escamilla@icf.unam.mx](mailto:luis.escamilla@icf.unam.mx)

† [ozulker17@itu.edu.tr](mailto:ozulker17@itu.edu.tr)

‡ [akarsuo@itu.edu.tr](mailto:akarsuo@itu.edu.tr)

§ [e.divalentino@sheffield.ac.uk](mailto:e.divalentino@sheffield.ac.uk)

¶ [javazquez@icf.unam.mx](mailto:javazquez@icf.unam.mx)

## II. WAVELET DEVIATIONS IN THE HUBBLE RADIUS

Wavelets are localized oscillatory functions, where “localized” means that they either have compact support or they approximate compact support by decaying rapidly.<sup>1</sup> In this paper, we will use them to write down Hubble radii,  $H^{-1}(z)$ , whose deviations from the Hubble radius of the  $\Lambda$ CDM model are wavelets. That is, for a given wavelet  $\psi(z)$ , we write

$$\frac{1}{H(z)} = \frac{1}{\mathcal{H}(z)} + \psi(z) \quad (1)$$

where  $\mathcal{H}(z)$  is the usual Hubble function of the  $\Lambda$ CDM model, which reads

$$3\mathcal{H}^2(z) = \rho_{m,0}(1+z)^3 + \rho_{r,0}(1+z)^4 + \rho_\Lambda, \quad (2)$$

with  $z$  being the redshift and  $\rho_i$  denoting the energy density of the matter (m), radiation (r), and cosmological constant ( $\Lambda$ ) components using the unit convention  $8\pi G = c = 1$ . Hereafter, the index “0” denotes the present-day value of any quantity. This framework implicitly assumes the Robertson-Walker (RW) metric from which the Hubble functions are defined, and as usual, the metric associated with the  $\Lambda$ CDM model is spatially flat.

These sorts of deviations from the Hubble radius of  $\Lambda$ CDM, defined by Eq. (1), were first considered in Ref. [183]. There, it was shown that for a given  $\mathcal{H}(z)$  in agreement with CMB measurements of the angular scale of the sound horizon at last scattering, any deviation in the Hubble radius that retains this agreement must be an admissible wavelet<sup>2</sup> unless the value of  $H_0$  and/or the comoving length of the sound horizon is also modified. It is crucial to clarify that, in the present paper, despite making use of the same wavelet framework described by Eq. (1), we do not require  $\mathcal{H}(z)$  itself to be in agreement with CMB measurements; rather, we simply use wavelets on top of  $\mathcal{H}(z)^{-1}$  to construct Hubble functions that oscillate around the functional form of  $\Lambda$ CDM due to the ability of wavelets to provide an arbitrary number of oscillations with a limited number of free parameters.

It is useful to relate the parameters of  $\mathcal{H}(z)$  and  $H(z)$ . A conveniently simple relation exists between the deceleration parameters of the Hubble functions, that is,

$$q(z) = \mathcal{Q}(z) + \frac{d\psi(z)}{dt}, \quad (3)$$

where  $q(z)$  and  $\mathcal{Q}(z)$  are the usual deceleration parameters for the metric solutions associated with  $H(z)$  and  $\mathcal{H}(z)$ , respectively. A special case of particular interest is a scenario where all of the deviations of  $H(z)$  from  $\mathcal{H}(z)$  arise due to a dynamical dark energy density,  $\rho_{\text{DE}}(z)$ , that replaces the  $\rho_\Lambda$  of the  $\Lambda$ CDM model, namely, the scenario with

$$3H^2(z) = \rho_{m,0}(1+z)^3 + \rho_{r,0}(1+z)^4 + \rho_{\text{DE}}(z). \quad (4)$$

Defining the normalized deviation between the Hubble functions,

$$\delta(z) \equiv \frac{H(z) - \mathcal{H}(z)}{\mathcal{H}(z)}, \quad (5)$$

one has

$$\rho_{\text{DE}}(z) = \rho_{\text{DE},0} + 3\mathcal{H}^2(z)\delta(z)[2 + \delta(z)]. \quad (6)$$

Moreover, we can obtain a DE equation of state (EoS) parameter as

$$w_{\text{DE}}(z) = -1 + \frac{2(1+z)\mathcal{H}^2}{\rho_{\text{DE}}} \left( \frac{\mathcal{H}'}{\mathcal{H}} \delta(\delta+2) + \delta'(\delta+1) \right), \quad (7)$$

and from here one can define the DE inertial mass density,  $\varrho_{\text{DE}} \equiv \rho_{\text{DE}}(1 + w_{\text{DE}})$ , which reads

$$\varrho_{\text{DE}}(z) = 2(1+z)\mathcal{H}^2 \left( \frac{\mathcal{H}'}{\mathcal{H}} \delta(\delta+2) + \delta'(\delta+1) \right), \quad (8)$$

where the prime denotes differentiation with respect to the redshift (we have dropped the redshift dependence of the functions for better readability).

Notice that, so far, we have not made any assumptions about  $\psi(z)$  other than it being a wavelet. A reliable way to obtain wavelets is by differentiating probability density functions. In parallel to Ref. [183], for the analyses in this paper, we will consider the family of Hermitian wavelets obtained from the derivatives of the Gaussian distribution—in fact, wavelets obtained from probability density functions generically satisfy the admissibility condition, which was a crucial point in Ref. [183], but not here. Let us define a Gaussian distribution

$$G(z) = -\frac{\alpha_h}{2\beta_h} e^{-\beta_h(z-z^\dagger)^2}, \quad (9)$$

where  $\beta_h > 0$  and  $\alpha_h$  can take any value, with the minus sign in front of the function being our convention (since this function can be negative depending on the sign of  $\alpha_h$ , strictly speaking, it is not a probability density function). Then, one can define a family of wavelets where the  $n^{\text{th}}$  member of the family corresponds to the  $n^{\text{th}}$  derivative of  $G(z)$  for  $n > 0$ , i.e.,

$$\psi_n(z) \equiv \frac{d^n G(z)}{dz^n}, \quad (10)$$

<sup>1</sup> This behavior can be observed in Fig. 1, where the deviations from  $\Lambda$ CDM (dashed line) characterized by underlying wavelets are oscillatory and approximately vanish outside of a finite range of redshift.

<sup>2</sup> Wavelets that satisfy the admissibility condition have a vanishing integral over their whole domain; hence, the angular diameter distance to the last scattering surface is preserved in the deviated scenario.

yielding

$$\psi_1(z) = -2\beta_h [z - z^\dagger] G(z), \quad (11a)$$

$$\psi_2(z) = 4\beta_h \left[ \beta_h (z - z^\dagger)^2 - \frac{1}{2} \right] G(z), \quad (11b)$$

$$\psi_3(z) = -8\beta_h^2 \left[ \beta_h (z - z^\dagger)^3 - \frac{3}{2} (z - z^\dagger) \right] G(z), \quad (11c)$$

$$\psi_4(z) = 16\beta_h^2 \left[ \beta_h^2 (z - z^\dagger)^4 - 3\beta_h (z - z^\dagger)^2 + \frac{3}{4} \right] G(z), \quad (11d)$$

and so on. This method of generating wavelets has the convenience of allowing one to control the number of nodes (crossings of zero) of the wavelet, hence the number of oscillations. While  $G(z)$  can be considered the zeroth-order wavelet, it has no nodes and does not oscillate. In comparison, every differentiation introduces one node to the wavelet, e.g.,  $\psi_1$  has a single node corresponding to one bump and one dip in the functional form; see Fig. 1. In the following sections, we make use of the first four Hermitian wavelets given in Eq. (11) to conduct our observational analyses.

### III. DATA SETS AND METHODOLOGY

To compare the standard model against our wavelet-extension of it, we will utilize the Bayesian framework in the form of a parameter inference procedure, which requires the use of data and a sampler code.

Our datasets consist of various combinations of observations related to the cosmic microwave background (CMB), baryon acoustic oscillations (BAO), type Ia supernovae (SN Ia) light curves, cosmic chronometers, and SN Ia absolute magnitudes. Specifically, the following data related to the above observations are used. We use the collection of 31 cosmic chronometers [184–190], found within the repository [191], in combination with the catalogue from the Pantheon+ SN Ia sample, covering a redshift range of  $0.001 < z < 2.26$  with 1701 light curves of 1550 distinguishable SN Ia [192]. The associated full covariance matrix is comprised of a statistical and a systematic part, which, along with the data, is provided in the repository [193]. These two datasets will always be used together and will be jointly referred to as **SN**. We employ two different BAO datasets. The first dataset contains SDSS, BOSS, and eBOSS surveys [16], in which the Lyman- $\alpha$  forest BAO measurements that cover a redshift up to  $z \approx 2.34$  are also included. This dataset will be referred to as **SB**, which stands for “SDSS-BAO”. The other dataset consists of BAO distance measurements from the first year of the Dark Energy Spectroscopic Instrument (DESI) [194], hereafter referred to as **DB** (for DESI-BAO); this dataset also includes Lyman- $\alpha$  measurements. To avoid double-counting, these measurements will not be combined with their **SB** counterparts; rather, we investigate in the next

section the consequences of using two different BAO datasets. In some instances, we will also use a Gaussian prior of  $H_0 = 73.04 \pm 1.04 \text{ km s}^{-1} \text{ Mpc}^{-1}$  from the local distance ladder measurements of the SH0ES team, relying on the calibration of the SN Ia absolute magnitude with Cepheid variables [27]. When this prior is in use, we denote it with the addition of **H0** in the name of the dataset combination. Finally, we will also make use of some background information from the Cosmic Microwave Background (CMB) from the Planck satellite in the form of a “BAO data point” at a redshift of  $z \sim 1100$ . The background-level information of the CMB can be encapsulated by the three parameters [170]:  $\omega_b$  (physical baryon density parameter),  $\omega_m$  (physical matter density parameter), and  $D_M(\sim 1100)/r_d$ , where  $r_d$  is the comoving size of the sound horizon at the drag epoch and  $D_M(z)$  is the comoving angular diameter distance to  $z$ . This dataset will be referred to as **Pl**.

To calculate the  $\chi^2$  for each data sample, we have

$$\chi_{\text{data}}^2 = (d_{i,m} - d_{i,\text{obs}})^T C_{ij,\text{data}}^{-1} (d_{j,m} - d_{j,\text{obs}}), \quad (12)$$

where  $d_m$  and  $d_{\text{obs}}$  are our model predictions and the observables, respectively, and  $C_{\text{data}}$  is the covariance matrix associated with each of the datasets. Since observations of each dataset are independent of each other, the joint  $\chi^2$  can be computed as

$$\chi_{\text{total}}^2 = \chi_{\text{Pl}}^2 + \chi_{\text{SN}}^2 + \chi_{\text{BAO}}^2 + \chi_{\text{H0}}^2, \quad (13)$$

where some terms may not be present depending on the dataset combination used, and the index of BAO will refer to either **SB** or **DB**.

For the determination of the optimal parameter values of our model, we employ an adapted version of a Monte Carlo Markov Chain (MCMC) code known as SimpleMC (see Ref. [195]). SimpleMC is designed to calculate expansion rates and distances based on a given Friedmann equation, allowing the analysis of the data at the background level. More information about the application of this code can be found in the Bayesian inference review presented in Ref. [196]. Additionally, our implementation uses **dynesty**, a nested sampling library described in Ref. [197], to efficiently compute the Bayesian evidence  $E(D|M)$ , where  $D$  is the data used and  $M$  is the sampled model. This evidence can be used to compare two distinct models by using the following relationship:

$$B_{12} \equiv \frac{E(D|M_1)}{E(D|M_2)}, \quad (14)$$

where  $B_{12}$  is known as the *Bayes Factor*, with  $M_1$  and  $M_2$  being the two models to be compared. By taking the natural logarithm of this quotient, together with the Jeffreys’ scale shown in Table I [198, 199], a useful empirical tool for performing model selection arises. That is, we can use it to gain insight into how well model  $M_1$  compares to model  $M_2$ .

This combination of tools enables us to perform parameter estimation and model comparison. Regarding

| $\ln B_{12}$ | Odds         | Probability | Strength of Evidence |
|--------------|--------------|-------------|----------------------|
| $< 1.0$      | $< 3:1$      | $< 0.75$    | Inconclusive         |
| 1.0          | $\sim 3:1$   | 0.750       | Weak Evidence        |
| 2.5          | $\sim 12:1$  | 0.923       | Moderate Evidence    |
| 5.0          | $\sim 150:1$ | 0.993       | Strong Evidence      |

TABLE I: Jeffreys’ scale for model selection based on the logarithm of the Bayes’ factor. A positive value of  $\ln B_{12}$  indicates evidence in favor of  $M_1$ , while a negative value indicates evidence in favor of  $M_2$ , following the convention from [198].

| Models                           | Priors                           |
|----------------------------------|----------------------------------|
| $\psi_1, \psi_2, \psi_3, \psi_4$ | $\beta_h : [0.01, 25.0]$         |
| $\psi_1, \psi_2, \psi_3, \psi_4$ | $z^\dagger : [0.0, 5.0]$         |
| $\psi_1$                         | $\alpha_h : [-0.01, 0.01]$       |
| $\psi_2$                         | $\alpha_h : [-0.001, 0.001]$     |
| $\psi_3$                         | $\alpha_h : [-0.0001, 0.0001]$   |
| $\psi_4$                         | $\alpha_h : [-0.00001, 0.00001]$ |

TABLE II: Flat prior ranges for the parameters of the Hermitian wavelets used in the analysis.

the flat priors used for the parameters of the model:  $\Omega_m = [0.1, 0.5]$  for the matter density parameter,  $\Omega_b h^2 = [0.02, 0.025]$  for the physical baryon density, and  $h = [0.4, 0.9]$  for the dimensionless reduced Hubble constant (where  $h = H_0/100 \text{ km s}^{-1} \text{ Mpc}^{-1}$ ). For the Hermitian wavelets, we need to be more careful with how we select our priors, and our selection requires some explanation.

As seen in Eq. (11), each Hermitian wavelet has three free parameters:  $\alpha_h$ ,  $\beta_h$ , and  $z^\dagger$ . Each parameter governs a distinct behavior of the wavelet: the parameter  $\alpha_h$  controls the amplitude; the parameter  $\beta_h$  controls both the “width” and the amplitude; and  $z^\dagger$  determines the center of the wavelet. For a visual reference, see Fig. 1, where we show the influence of each parameter on  $H(z)/(1+z)$ . One important thing to note is that the sensitivity of the amplitude of wavelets with respect to the parameter  $\alpha_h$  increases with higher-order wavelets. Thus, its prior range diminishes by an order of magnitude when going from  $\psi_i$  to  $\psi_{i+1}$ . Therefore, our priors for each parameter are:  $\beta_h : [0.01, 25.0]$  and  $z^\dagger : [0.0, 5.0]$  for every wavelet; meanwhile, we will set  $\alpha_h : [-0.01, 0.01]$  for  $\psi_1$ ,  $\alpha_h : [-0.001, 0.001]$  for  $\psi_2$ ,  $\alpha_h : [-0.0001, 0.0001]$  for  $\psi_3$ , and  $\alpha_h : [-0.00001, 0.00001]$  for  $\psi_4$  (for reference, they can be found in Table II).

#### IV. RESULTS

In this section, we present the results of our sampling process, with a particular focus on the differences between the two BAO datasets. Due to the high number of dataset combinations used, we visualize only a selection of the plots and comment on the others as necessary. For

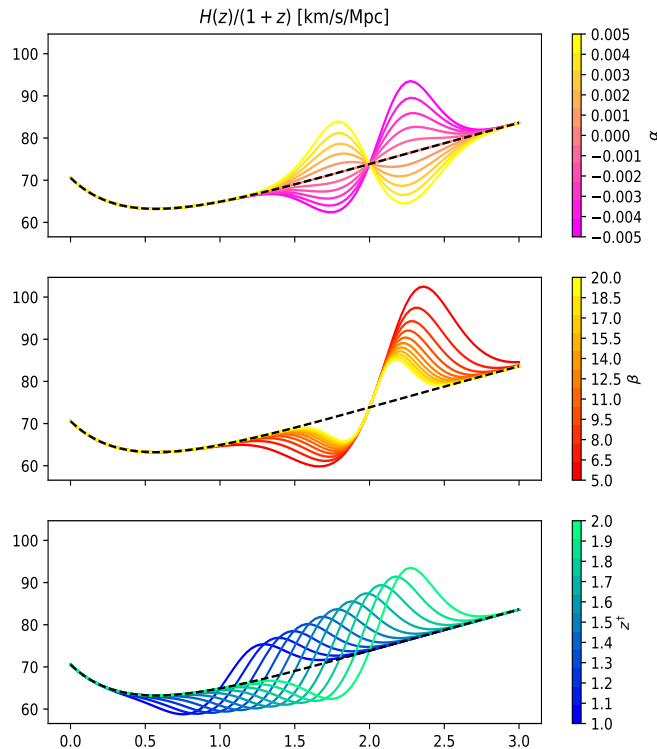


FIG. 1: Visual representation of how the underlying Hermitian wavelet (specifically  $\psi_1$ ) affects the co-moving Hubble parameter  $H(z)/(1+z)$ , where  $H(z) = \frac{H_{\Lambda\text{CDM}}(z)}{1+\psi(z)H_{\Lambda\text{CDM}}(z)}$ , when varying each parameter individually. The upper plot corresponds to the parameter  $\alpha_h$  in the interval  $[-0.005, 0.005]$ , the middle one to  $\beta_h = [5, 20]$ , and the lower one to  $z^\dagger = [1.0, 2.0]$ . The black dashed line represents  $H_{\Lambda\text{CDM}}(z)/(1+z)$ .

completeness, the best-fit values of  $h$  and  $\Omega_{m,0}$ , as well as the Bayes’ factors and  $-2\Delta \ln \mathcal{L}_{\text{max}}$ , for all analyses are provided in Tables III and IV.

In Fig. 2, we plot the 1D marginalized posterior distributions of  $z^\dagger$  for the first-order wavelet  $\psi_1$ . While we show only one wavelet, similar features are observed across the others (see Appendix A and Fig. A.1). A notable feature is the absence of a clear peak in the posterior distribution without BAO data, as seen in the leftmost panel. This situation changes in the middle panel with the inclusion of **SB**, where a distinct peak around  $z^\dagger \sim 2.5$  appears when **PI** is not included (red and green plots). When **PI** is also included, a bimodal distribution is observed, with a smaller peak around  $z^\dagger \sim 1$  and a larger accumulation of probability for  $z^\dagger \gtrsim 3$ . It is important to note that **PI** is the only dataset used beyond the redshift of 2.34, and the impact of a wavelet at high redshifts does not lead to significant differences when compared with any combination of BAO, **SN**, or **H0** data. Moreover, even **PI** is not affected by a high redshift wavelet as we only do a background analysis for which admissible wavelets induce no changes over  $\Lambda\text{CDM}$  when CMB data is considered (see Ref. [183]). In fact, a high redshift wavelet well-approximates  $\Lambda\text{CDM}$  where

| Model               | Data Sets          | $h$           | $\Omega_{m,0}$ | $\ln B_{\Lambda\text{CDM},i}$ | $-2\Delta \ln \mathcal{L}_{\text{max}}$ |
|---------------------|--------------------|---------------|----------------|-------------------------------|---|
| $\Lambda\text{CDM}$ | <b>SB+PI</b>       | 0.679 (0.006) | 0.309 (0.007)  | 0                             | 0                                       |
| $\psi_1$            |                    | 0.688 (0.006) | 0.301 (0.007)  | -0.69 (0.34)                  | -5.08                                   |
| $\psi_2$            |                    | 0.688 (0.006) | 0.302 (0.008)  | -1.02 (0.35)                  | -4.94                                   |
| $\psi_3$            |                    | 0.689 (0.006) | 0.301 (0.007)  | -0.89 (0.35)                  | -4.54                                   |
| $\psi_4$            |                    | 0.689 (0.006) | 0.301 (0.008)  | -0.75 (0.34)                  | -4.81                                   |
| $\Lambda\text{CDM}$ | <b>SB+SN</b>       | 0.686 (0.013) | 0.306 (0.013)  | 0                             | 0                                       |
| $\psi_1$            |                    | 0.692 (0.014) | 0.315 (0.015)  | -0.61 (0.17)                  | -7.42                                   |
| $\psi_2$            |                    | 0.692 (0.014) | 0.318 (0.016)  | -1.22 (0.17)                  | -8.59                                   |
| $\psi_3$            |                    | 0.693 (0.014) | 0.315 (0.015)  | -0.83 (0.18)                  | -8.07                                   |
| $\psi_4$            |                    | 0.692 (0.014) | 0.314 (0.014)  | -0.71 (0.18)                  | -8.61                                   |
| $\Lambda\text{CDM}$ | <b>SB+SN+PI</b>    | 0.676 (0.006) | 0.312 (0.007)  | 0                             | 0                                       |
| $\psi_1$            |                    | 0.684 (0.005) | 0.306 (0.007)  | -0.22 (0.35)                  | -5.22                                   |
| $\psi_2$            |                    | 0.685 (0.005) | 0.306 (0.006)  | -0.51 (0.34)                  | -4.72                                   |
| $\psi_3$            |                    | 0.684 (0.005) | 0.307 (0.007)  | -0.54 (0.34)                  | -5.29                                   |
| $\psi_4$            |                    | 0.685 (0.006) | 0.306 (0.007)  | -0.66 (0.34)                  | -6.58                                   |
| $\Lambda\text{CDM}$ | <b>SB+SN+H0</b>    | 0.709 (0.014) | 0.311 (0.013)  | 0                             | 0                                       |
| $\psi_1$            |                    | 0.705 (0.012) | 0.315 (0.015)  | 0.14 (0.24)                   | -2.91                                   |
| $\psi_2$            |                    | 0.706 (0.012) | 0.318 (0.015)  | 0.34 (0.24)                   | -3.17                                   |
| $\psi_3$            |                    | 0.705 (0.012) | 0.314 (0.015)  | 0.55 (0.23)                   | -3.89                                   |
| $\psi_4$            |                    | 0.705 (0.011) | 0.314 (0.015)  | -0.11 (0.23)                  | -3.23                                   |
| $\Lambda\text{CDM}$ | <b>SB+SN+PI+H0</b> | 0.679 (0.005) | 0.308 (0.007)  | 0                             | 0                                       |
| $\psi_1$            |                    | 0.687 (0.005) | 0.303 (0.007)  | -1.38 (0.34)                  | -6.18                                   |
| $\psi_2$            |                    | 0.688 (0.005) | 0.302 (0.007)  | -1.52 (0.34)                  | -6.34                                   |
| $\psi_3$            |                    | 0.688 (0.006) | 0.302 (0.007)  | -1.48 (0.35)                  | -7.16                                   |
| $\psi_4$            |                    | 0.688 (0.005) | 0.302 (0.006)  | -1.21 (0.34)                  | -7.78                                   |
| $\Lambda\text{CDM}$ | <b>SN+PI</b>       | 0.671 (0.006) | 0.319 (0.008)  | 0                             | 0                                       |
| $\psi_1$            |                    | 0.681 (0.006) | 0.311 (0.008)  | -0.02 (0.34)                  | -2.82                                   |
| $\psi_2$            |                    | 0.681 (0.006) | 0.309 (0.008)  | 0.22 (0.35)                   | -3.53                                   |
| $\psi_3$            |                    | 0.681 (0.006) | 0.310 (0.008)  | 0.52 (0.34)                   | -3.54                                   |
| $\psi_4$            |                    | 0.681 (0.006) | 0.310 (0.008)  | 0.28 (0.35)                   | -4.42                                   |
| $\Lambda\text{CDM}$ | <b>SN+PI+H0</b>    | 0.675 (0.006) | 0.314 (0.008)  | 0                             | 0                                       |
| $\psi_1$            |                    | 0.685 (0.006) | 0.306 (0.007)  | -0.61 (0.34)                  | -5.56                                   |
| $\psi_2$            |                    | 0.685 (0.006) | 0.306 (0.007)  | -0.69 (0.35)                  | -6.51                                   |
| $\psi_3$            |                    | 0.685 (0.006) | 0.306 (0.008)  | -0.82 (0.35)                  | -6.27                                   |
| $\psi_4$            |                    | 0.684 (0.006) | 0.306 (0.007)  | -0.85 (0.35)                  | -6.37                                   |

TABLE III: First half of the mean values and standard deviations for two of the parameters used in the reconstruction,  $\Omega_{m,0}$  and  $h$ . For each model, the last two columns present the natural logarithm of the Bayes Factor,  $\ln B_{\Lambda\text{CDM},i}$ , and  $-2\Delta \ln \mathcal{L}_{\text{max}}$ , defined as  $-2\ln(\mathcal{L}_{\text{max},i}/\mathcal{L}_{\text{max},\Lambda\text{CDM}})$ , for a comparison of the fit of the data. When BAO data is included, it is denoted as **SB** in this table.

data are present; this can be seen by comparing, say, the rightmost panel of Fig. 3 with Fig. 1, where the shape of the  $\Lambda\text{CDM}$  curve can be seen in dashed lines. Since the **PI** data is also not sensitive to high-redshift wavelets, we interpret the change in the posterior of  $z^\dagger$  to be due to the restrictions imposed by **PI** on the baseline  $\Lambda\text{CDM}$  parameters ( $\Omega_m$ ,  $h$ , and  $\Omega_b h^2$ ), which in turn, cannot be combined with a wavelet at low redshifts in the presence of low-redshift data. This restriction on the baseline parameters becomes evident by comparing the third and fourth panels of Fig. 3, where the  $\Lambda\text{CDM}$ -like curves be-

| Model               | datasets           | $h$           | $\Omega_{m,0}$ | $\ln B_{\Lambda\text{CDM},i}$ | $-2\Delta \ln \mathcal{L}_{\text{max}}$ |
|---------------------|--------------------|---------------|----------------|-------------------------------|---|
| $\Lambda\text{CDM}$ | <b>DB+PI</b>       | 0.677 (0.006) | 0.311 (0.008)  | 0                             | 0                                       |
| $\psi_1$            |                    | 0.686 (0.008) | 0.304 (0.009)  | -0.82 (0.34)                  | -8.18                                   |
| $\psi_2$            |                    | 0.686 (0.006) | 0.303 (0.008)  | -0.78 (0.33)                  | -10.12                                  |
| $\psi_3$            |                    | 0.687 (0.006) | 0.303 (0.007)  | -0.84 (0.32)                  | -10.24                                  |
| $\psi_4$            |                    | 0.688 (0.006) | 0.302 (0.007)  | -0.81 (0.34)                  | -10.48                                  |
| $\Lambda\text{CDM}$ | <b>DB+SN</b>       | 0.683 (0.017) | 0.313 (0.012)  | 0                             | 0                                       |
| $\psi_1$            |                    | 0.679 (0.014) | 0.309 (0.012)  | -0.12 (0.23)                  | -11.42                                  |
| $\psi_2$            |                    | 0.681 (0.013) | 0.308 (0.012)  | -0.21 (0.23)                  | -11.08                                  |
| $\psi_3$            |                    | 0.679 (0.014) | 0.308 (0.012)  | 0.05 (0.24)                   | -10.92                                  |
| $\psi_4$            |                    | 0.679 (0.013) | 0.309 (0.012)  | 0.02 (0.22)                   | -11.22                                  |
| $\Lambda\text{CDM}$ | <b>DB+SN+PI</b>    | 0.675 (0.005) | 0.314 (0.007)  | 0                             | 0                                       |
| $\psi_1$            |                    | 0.683 (0.005) | 0.308 (0.007)  | 0.01 (0.32)                   | -11.61                                  |
| $\psi_2$            |                    | 0.683 (0.005) | 0.307 (0.007)  | 0.05 (0.33)                   | -10.11                                  |
| $\psi_3$            |                    | 0.683 (0.006) | 0.307 (0.007)  | -0.21 (0.32)                  | -10.65                                  |
| $\psi_4$            |                    | 0.683 (0.005) | 0.308 (0.007)  | 0.15 (0.31)                   | -10.25                                  |
| $\Lambda\text{CDM}$ | <b>DB+SN+H0</b>    | 0.702 (0.014) | 0.311 (0.012)  | 0                             | 0                                       |
| $\psi_1$            |                    | 0.703 (0.013) | 0.311 (0.011)  | -0.14 (0.27)                  | -11.33                                  |
| $\psi_2$            |                    | 0.704 (0.013) | 0.312 (0.011)  | -0.31 (0.23)                  | -10.86                                  |
| $\psi_3$            |                    | 0.703 (0.013) | 0.311 (0.011)  | -0.67 (0.26)                  | -10.14                                  |
| $\psi_4$            |                    | 0.704 (0.013) | 0.311 (0.012)  | -0.56 (0.25)                  | -10.81                                  |
| $\Lambda\text{CDM}$ | <b>DB+SN+PI+H0</b> | 0.678 (0.005) | 0.311 (0.007)  | 0                             | 0                                       |
| $\psi_1$            |                    | 0.686 (0.005) | 0.304 (0.007)  | -1.61 (0.35)                  | -13.25                                  |
| $\psi_2$            |                    | 0.686 (0.005) | 0.304 (0.007)  | -1.41 (0.34)                  | -11.87                                  |
| $\psi_3$            |                    | 0.686 (0.005) | 0.304 (0.006)  | -1.99 (0.34)                  | -12.48                                  |
| $\psi_4$            |                    | 0.686 (0.005) | 0.304 (0.007)  | -1.31 (0.34)                  | -12.01                                  |
| $\Lambda\text{CDM}$ | <b>SN</b>          | 0.674 (0.027) | 0.331 (0.017)  | 0                             | 0                                       |
| $\psi_1$            |                    | 0.676 (0.026) | 0.331 (0.017)  | 0.58 (0.23)                   | -3.71                                   |
| $\psi_2$            |                    | 0.675 (0.026) | 0.332 (0.018)  | 0.12 (0.24)                   | -3.85                                   |
| $\psi_3$            |                    | 0.676 (0.028) | 0.332 (0.018)  | 0.13 (0.22)                   | -5.21                                   |
| $\psi_4$            |                    | 0.676 (0.026) | 0.330 (0.017)  | 0.42 (0.23)                   | -5.41                                   |
| $\Lambda\text{CDM}$ | <b>SN+H0</b>       | 0.711 (0.019) | 0.322 (0.017)  | 0                             | 0                                       |
| $\psi_1$            |                    | 0.711 (0.017) | 0.323 (0.016)  | -0.28 (0.22)                  | -3.88                                   |
| $\psi_2$            |                    | 0.712 (0.017) | 0.323 (0.017)  | -0.12 (0.22)                  | -4.18                                   |
| $\psi_3$            |                    | 0.712 (0.017) | 0.324 (0.016)  | -0.69 (0.22)                  | -5.04                                   |
| $\psi_4$            |                    | 0.712 (0.018) | 0.322 (0.017)  | -0.09 (0.24)                  | -5.66                                   |

TABLE IV: Second half of the mean values and standard deviations for two of the parameters used in the reconstruction,  $\Omega_{m,0}$  and  $h$ . In this table, when BAO data is included, it is denoted as **DB**. For each model, the last two columns present the natural logarithm of the Bayes Factor,  $\ln B_{\Lambda\text{CDM},i}$ , and  $-2\Delta \ln \mathcal{L}_{\text{max}}$ , defined as  $-2\ln(\mathcal{L}_{\text{max},i}/\mathcal{L}_{\text{max},\Lambda\text{CDM}})$ , for a comparison of the fit of the data.

come denser resulting in the removal of some freedom in the expansion history. Finally, we note that the inclusion of **H0** in the dataset has almost no impact on the constraints on  $z^\dagger$  with or without **SB**.

Moving on to the last panel of Fig. 2, we see that when **DB** is included instead of **SB**, the results are more stable with respect to the addition of **PI** and the bimodal distribution is present for all dataset combinations. More interestingly, the peak at low redshifts moves to around  $z^\dagger \sim 0.7$  and the inclusion of the **SN** data strengthens this peak, significantly decreasing the probability around

a  $\Lambda$ CDM-like cosmology within the redshift range where data are present. This result is in line with the findings of the DESI collaboration in Ref. [194] that note a  $\sim 2.6\sigma$  preference for dynamical DE (when the DE is allowed to evolve with the Chevallier-Polarski-Linder parametrization) when DESI-BAO is combined with CMB data, which goes up to  $\sim 3.9\sigma$  when SN Ia data are also included; however, note that they still find only  $\sim 2.5\sigma$  evidence when their chosen SN Ia dataset is Pantheon+ (in comparison to Union3 [200] or DESY5 [201]), whereas, here we find that the preference for a dynamical DE [if the wavelets are assumed to originate from a dynamical DE component as described by Eq. (6)] is strengthened with the inclusion of **SN** that consists of Pantheon+ and cosmic chronometers. And as before, the constraints on  $z^\dagger$  are not very sensitive to the inclusion of **H0**.

Regarding the constraints on the parameters  $\alpha_h$  and  $\beta_h$ , we consider these results to be less relevant (especially when compared to  $z^\dagger$ ) for inclusion in the main text. However, their 1D posteriors and a brief discussion can be found in Appendix A.

In Fig. 3 (see also Fig. A.4), we show the Hubble functions corresponding to  $\psi_1$  for BAO+**SN** dataset combinations with and without **PI**, and using both **SB** and **DB**. In a similar manner to the 1D posterior plots for  $z^\dagger$ , we limit this discussion to  $\psi_1$  since the behaviors are similar across all wavelets, as shown in Fig. A.5.. Again, we see the lower-redshift dynamics preferred by **DB** with  $z^\dagger \sim 0.7$  in comparison to the preference for higher  $z^\dagger$  values by **SB**. The inclusion of **PI** causes the  $\Lambda$ CDM parameters to be strictly constrained, and when **SB** is present, in contrast to the **DB** case, it also pushes the wavelets to redshifts mostly irrelevant to our low-redshift datasets. We see that the presence of the wavelets allows a better fit to the BAO data as argued in Ref. [183]. However, the  $D_H(z)/r_d$  values from the BAO data are accompanied also by  $D_M(z)/r_d$  values (also  $D_V(z)/r_d$ , but we do not discuss them).<sup>3</sup> In Fig. 4, we also plot the inverted and scaled  $D_M(z)$  function for  $\psi_1$  for the dataset combination selected in the second panel of Fig. 3. It is clear from Figs. 3 and 4 that even for this case, where the oscillatory features of wavelets are readily apparent in the  $H(z)/(1+z)$  plots, the  $D_M(z)$  function is barely affected by the wavelets. This is due to the  $D_M(z)$  function being an integral of the Hubble radius which smooths out the wavelet deviations. Thus, we can safely argue that it is the  $D_H(z)/r_d$  measurements from the BAO data that drive the preference for wavelets and not the  $D_M(z)/r_d$  measurements. In particular, Fig. 3 indicates that it is the Lyman- $\alpha$   $D_H(z)/r_d$  measurement for **SB**, and the  $D_H(z)/r_d$  measurement at  $z = 0.51$  for the **DB** with the ‘‘anomalous’’  $D_M(z)/r_d$  measurement of **DB** having little to no effect in driving the wavelets.

As shown in Tables III and IV, while the early universe constraints on the matter density and the Hubble constant remain unchanged, every case with wavelets provides a better fit to the data, as indicated by the negative  $-2\Delta \ln \mathcal{L}_{\max}$  values. This improvement exceeds the expected  $-3$  difference due to the additional three free parameters associated with the wavelets compared to  $\Lambda$ CDM. Notably, when using **DB**, wavelets are favored at over  $3\sigma$  ( $\sqrt{\Delta \chi^2}$ ) in all cases except one ( $\psi_1$  with **DB+PI**, as seen in Table IV), even with the Planck likelihood.<sup>4</sup> This advantage diminishes when **SB** is used as the BAO dataset. This is impressive as the Planck likelihood imposes heavy restrictions on both  $\Omega_{m,0}$  and  $h$  (as seen in their inferred values and  $1\sigma$  when the **PI** dataset is present and in Fig. 3 when **PI** is used) and this in turn could act against our wavelet extension of the standard model. A clear way to verify this is by analyzing Fig. 2. When the Planck likelihood is present, we observe a rise of an apparent bimodality centered in  $z^\dagger \sim 4$ . Given the fact that our data spans a redshift up to 2.34, if the wavelet is centered way beyond this point (which in this case means centered in  $z > 3$ ), we can assume that the datasets used for the parameter inference stand against the inclusion of the wavelet in the redshift interval covered by them. This is especially true when SDSS-BAO is included, although not with DESI-BAO, which can be verified by referring back to Fig. 3 and the  $\Delta \ln \mathcal{L}_{\max}$  values in Tables III and IV. By looking at these functional posteriors, it is clear that, when using **SB** (**DB**), the center of the wavelet is localized in  $z \sim 2.3$  ( $z \sim 0.7$ ), and by adding **PI**, we observe that the wavelet behavior is fully displaced with  $\Lambda$ CDM-like behavior and unconstrained when **SB** is present.

Focusing now on the Bayesian evidence through the Bayes’ factor  $\ln B_{\Lambda\text{CDM},i}$  in Tables III and IV, we can see some interesting results. Almost every case is as good ( $|\ln B| < 1$ ) or better (with weak evidence in favor of the wavelets according to Jeffreys’ scale) than the standard model at explaining the data. The best cases obtained are **DB+SN+PI+H0** and **SB+SN+PI+H0**, the reason being that a wavelet-like behavior seems to be a good alternative to  $\Lambda$ CDM at reconciling the localized dynamical behavior preferred by both of the different BAO datasets while preserving the good fit of  $\Lambda$ CDM to the measurements of the first peak of the CMB power spectrum.

Let us investigate the results for a specific dataset combination to see the effect that the SDSS-BAO likelihood has, and to show the similar behavior of our wavelets of different orders. This case will be **SB+SN**, which presents a great fit of the data (the best out of all the **SB** cases) and relatively good Bayes’ factors for every wavelet (all negative). The parameter  $z^\dagger$  strongly favors values around  $z = 2.3$ . The specific values (with their

<sup>3</sup> For reference, we note that  $D_H(z) = c/H(z)$ ,  $D_M(z) = c \int_0^z dz'/H(z')$  for a spatially flat RW metric, and  $D_V(z) = [zD_M(z)^2 D_H(z)]^{1/3}$ .

<sup>4</sup> This is again in line with the findings of the DESI collaboration as explained in the previous paragraph of the main text.

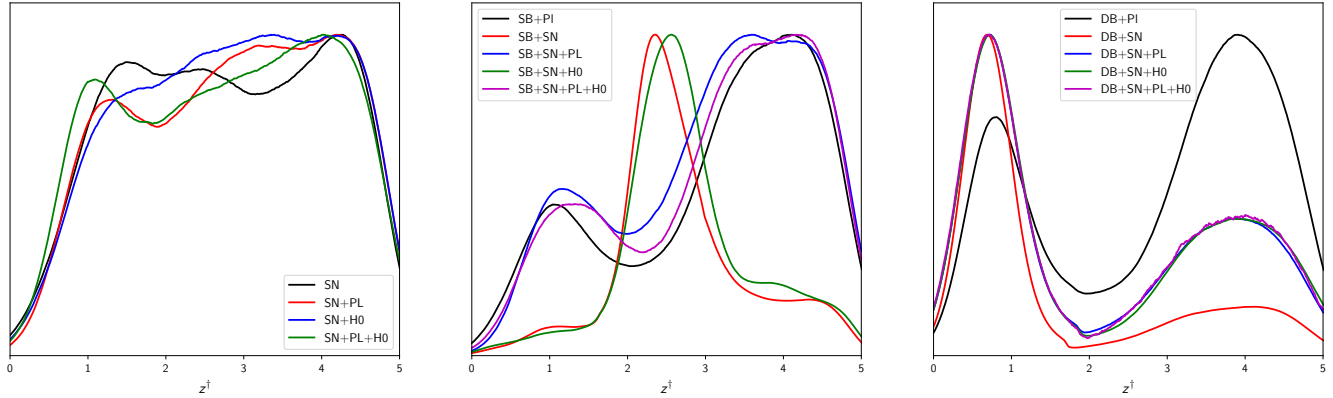


FIG. 2: 1D marginalized posterior distributions for the reconstructed parameter  $z^\dagger$  for  $\psi_1(z)$ . We present the results in three different panels to show the effect of BAO datasets on the posteriors. These plots were made using the Python library `getdist` [202].

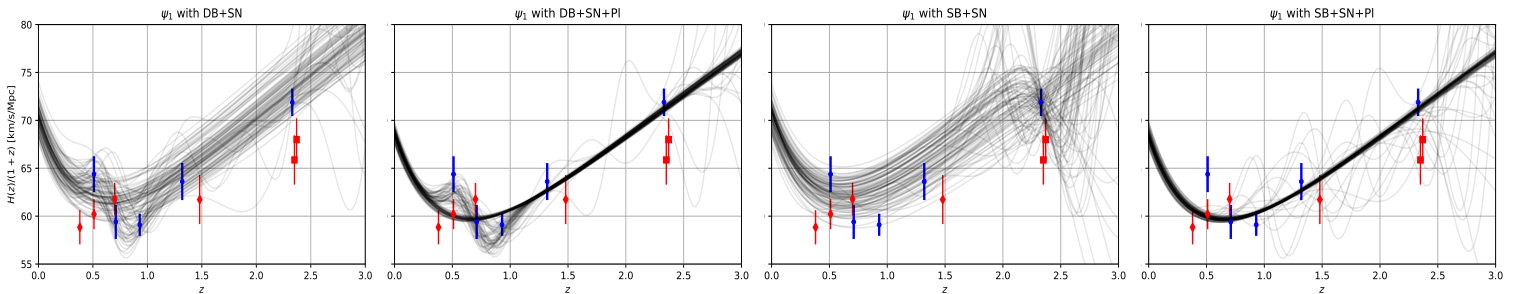


FIG. 3: Functional posterior for  $H(z)/(1+z)$  for  $\psi_1(z)$  using four distinct data combinations: **DB+SN**, **DB+SN+PI**, **SB+SN**, and **SB+SN+PI**. The red (blue) error bars correspond to the SDSS (DESI) BAO distance  $D_H(z)/r_d$  measurements. The size of the sound horizon was fixed to the robust value of 147 Mpc to show the BAO data in the figure. The plots were made using the Python library `fgivenx` [203].

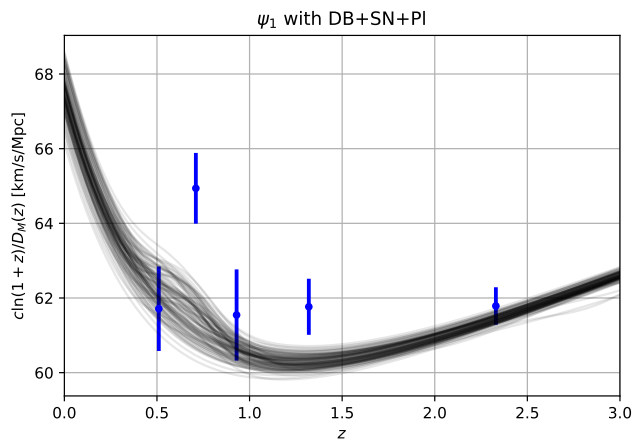


FIG. 4: Functional posterior of the inverted and scaled comoving angular diameter distance,  $c \ln(1+z)/D_M(z)$ , where  $D_M(z) = c \int_0^z dz'/H(z')$ ; note that this scaled function approaches  $H_0$  as  $z \rightarrow 0$ . The blue error bars correspond to the re-scaled  $D_M$  measurements from DESI, and the functional posterior was made with the reconstructed wavelet of first order,  $\psi_1$ , using the dataset combination **DB+SN+PI**. The size of the sound horizon was fixed to the robust value of 147 Mpc to show the BAO data in the figure. The plot was made using the Python library `fgivenx` [203].

$1\sigma$  uncertainties) are:  $2.4 \pm 1.0$  for  $\psi_1$ ,  $2.44 \pm 0.92$  for  $\psi_2$ ,  $2.48 \pm 0.96$  for  $\psi_3$ , and  $2.52 \pm 0.98$  for  $\psi_4$ . When examining the functional posteriors depicted in Fig. 5 concerning  $H(z)/(1+z)$ , the impact of the wavelets around  $z \sim 2.4$  becomes evident. It can be deduced that the primary dataset influencing the positioning of our wavelets is the high-redshift Lyman- $\alpha$  BAO data given that it is localized at  $z = 2.34$ . This behavior directly translates to the DE density as a possible transition from positive at low redshifts to negative at high redshifts as seen in Fig. 5. This is particularly accentuated by the best-fits (red-dashed lines in Fig. 5) of wavelets  $\psi_2$  and  $\psi_4$ , which have the lowest  $-2\Delta \ln \mathcal{L}_{\max}$  overall (for the cases with **SB** in the datasets). This transition to a negative value is accentuated by the DE EoS parameter since it presents a pole ( $\lim_{z \rightarrow z_p^\pm} w_{\text{DE}}(z) = \pm\infty$  with  $z_p$  being the point where DE density vanishes) when using the best-fit values (dashed red lines in Fig. 5) close to  $z = 2.5$ . This pole and asymptotic behavior have been observed in previous works considering effective DE densities changing sign [73, 79, 89, 98, 100, 104, 125, 134, 154, 160, 169, 171, 175, 183, 204–214] and its presence is required when the DE density changes sign for a conserved DE [214].

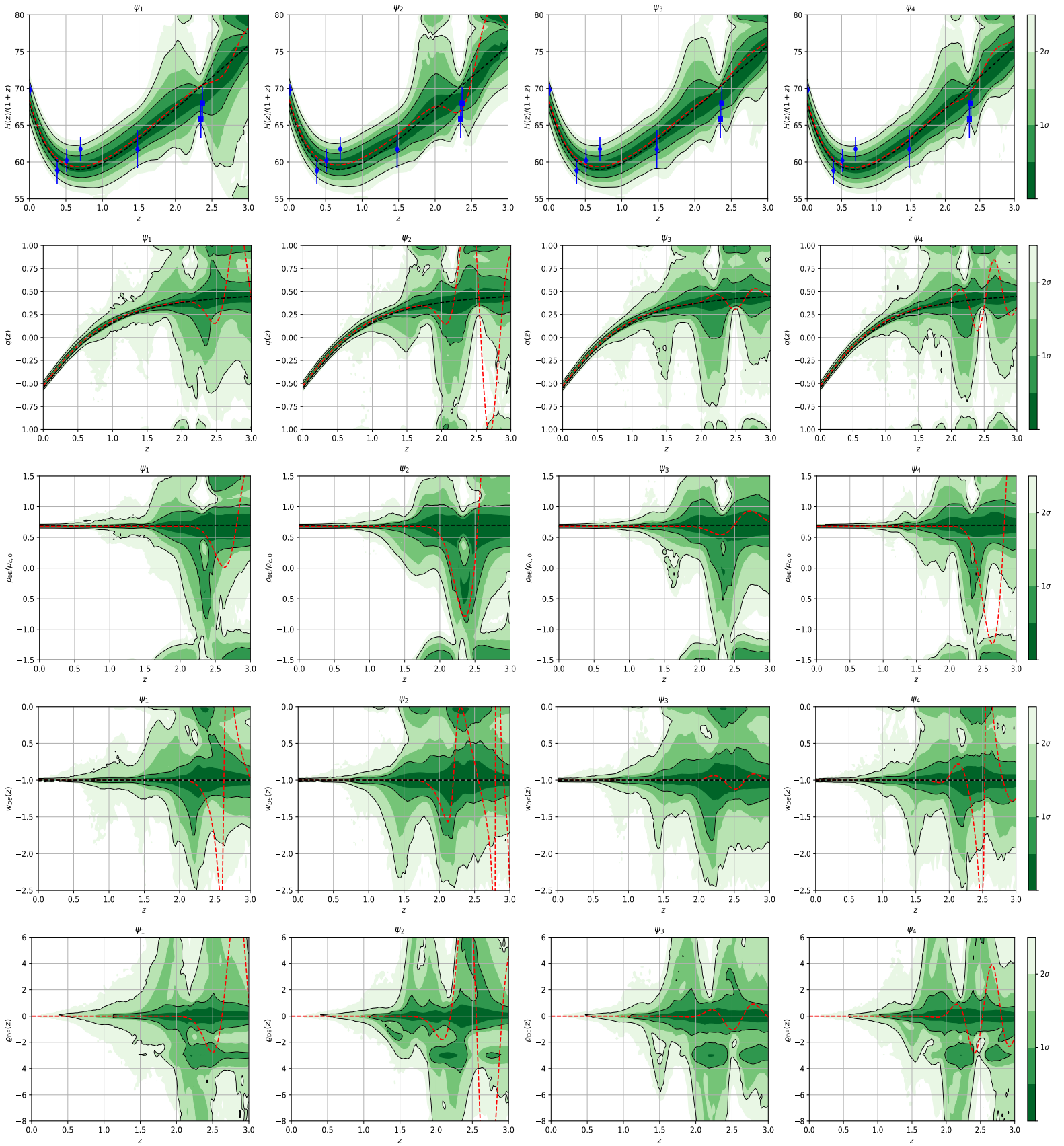


FIG. 5: Functional posterior probability of  $H(z)/(1+z)$ ,  $q(z)$ ,  $\rho_{DE}(z)/\rho_{c,0}$ ,  $w_{DE}(z)$ , and  $g_{DE}(z)$  for the datasets **SB+SN**. The probability, normalized in each slice of constant  $z$ , is shown with a color scale representing confidence interval values. The 68% ( $1\sigma$ ) and 95% ( $2\sigma$ ) confidence intervals are plotted as black lines. The dashed black line corresponds to the standard  $\Lambda$ CDM values, and the dashed red line represents the best-fit values of the wavelets. These plots were made using the Python library `fgivenx` [203].



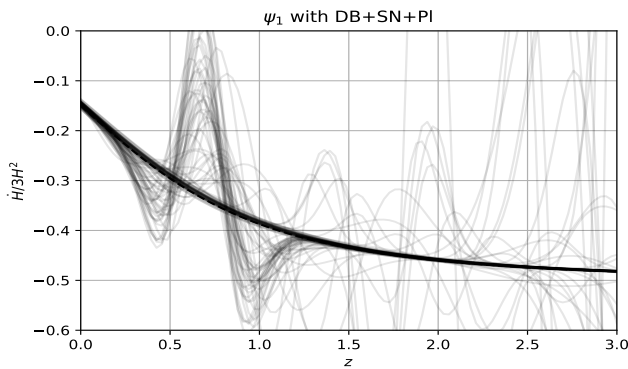


FIG. 6: Functional posterior of the time derivative of the Hubble parameter,  $\dot{H}$ , normalized by the critical density,  $3H^2$ . The functional posterior was made with the reconstructed wavelet of first order,  $\psi_1$ , using the dataset combination **DB+SN+PI**. The plot was made using the Python library `fgivenx` [203].

This feature of the DE density being able to attain negative values while also being able to oscillate makes the DE source derived from the wavelets a member of the omnipotent DE family [113].

However, even though Hermitian wavelets seem to be a good extension for the standard model, we cannot ignore how their influence translates into the deceleration parameter  $q(z)$ , which exhibits strong oscillatory behavior, especially with  $\psi_2$ . This would imply significant changes in the dynamics of the Universe, directly affecting structure formation [1, 2, 215–217]. These heavy oscillations are also evident in the DE density. The primary cause for this is the fact that the parameter  $\beta_h$  (which has a direct impact on the width and amplitude of the oscillations) is not constrained due to the lack of data beyond  $z = 2.34$ . To fully resolve this issue, we would require data that covers a larger region of redshift so that  $\beta_h$  can be fully characterized. Beyond  $z = 2.5$ , we can only speculate about the possible behavior of the wavelets. Despite this issue, it is clear that **SB** prefers the Hermitian wavelet to exert its influence beyond  $z \sim 1.5$ .

Finally, we comment on the time derivative of the Hubble function as plotted in Fig. 6. When all the modifications to the Friedmann equations can be absorbed in the total energy density ( $\rho$ ) and pressure ( $p$ ) components of the energy-momentum tensor, this time derivative reads

$$\dot{H} = -\frac{1}{2}(\rho + p), \quad (15)$$

where the dot denotes differentiation with respect to cosmic time. Notice that the total inertial mass density  $\varrho = \rho + p$  we discuss here is different from the DE inertial mass density,  $\varrho_{\text{DE}}$ , shown in the last row of Fig. 5. Plotting Eq. (15) is of interest since if  $\dot{H}$  is positive, the null energy condition is violated by the total energy-momentum content (which might include effective components originating from, say, a modified theory of gravity) of the Universe. The violation of the null energy condition and even the averaged null energy condition are

abundant in physics; see the discussions and references in Refs. [214, 218–221]. As seen in the example case presented in Fig. 6 (corresponding to the case in Fig. 4 and the second panel of Fig. 3), some of the plotted lines from the posterior become positive at certain redshifts, indicating a violation of the null energy condition. However, this behavior is not present in most of the samples and is not accentuated enough to make any claims regarding a preference for this behavior from the available data. Moreover, we would expect the presence of this violation within the wavelet framework to be highly dependent on the type of wavelet that is chosen; e.g., a more squarely shaped wavelet would induce more abrupt oscillations in the Hubble parameter, causing this violation to be much more common in its constrained parameter space.

## V. CONCLUSIONS

In this paper, we used a parameter inference procedure to analyze the behaviors of the Hubble function as preferred by background cosmological data. In this regard, we parameterized the Hubble function by considering deviations from the Hubble radius of  $\Lambda$ CDM in the form of wavelets as discussed in Ref. [183]. Wavelets provide viable extensions of the  $\Lambda$ CDM model while preserving some features of it, such as the size of the comoving sound horizon and the fit to the measurement of its angular scale at last scattering.

All our reconstructions present a significant improvement in the fit to the data, reaching more than  $3\sigma$  indication for wavelets when including DESI-BAO data. Most cases even present a negative Bayes' factor, indicating inconclusive or weak evidence in favor of wavelets (according to Jeffreys' Scale), despite having three extra parameters. In line with the discussions in Ref. [183], a dataset that exerts great influence on the behavior of the wavelets is BAO, which can dictate where the wavelet will be localized. DESI-BAO prefers the center of the wavelets to be at  $z \sim 0.7$ , while SDSS-BAO pushes it to  $z \sim 2.3$ . Our results indicate that this behavior is driven by differences between the  $D_H(z)/r_d$  measurements of the two BAO datasets at  $z < 1$  and  $z \sim 2.3$ , in particular, the discrepancy between the SDSS and DESI measurements at  $z = 0.51$  and in their Lyman- $\alpha$  BAO measurements. This discrepancy between BAO datasets could be due to statistical fluctuations, but it is beyond the scope of this work to explore its cause. We also note that the improvement in the fit compared to  $\Lambda$ CDM is significantly larger for the DESI-BAO compared to SDSS, and the addition of our **SN** dataset slightly ameliorates these improvements in line with the findings of the DESI collaboration for a preference of dynamical DE with BAO and SN Ia data [194].

We also showed how other derived quantities such as  $q(z)$ ,  $\rho_{\text{DE}}$ , and  $w_{\text{DE}}$  would behave and what effects the wavelets could have, particularly when SDSS-BAO is used. When the wavelet deviations are assumed to origi-

nate from a dynamical DE component, this DE presents some previously studied behaviors such as oscillations and a possible transition from a positive DE energy density to a negative one as redshift increases, making this DE a member of the omnipotent DE [113] family characterized by the combination of these two behaviors. While oscillations are present in  $\rho_{\text{DE}}$  by construction due to the oscillatory behaviors of the wavelets, the DE density attaining negative values in the past is a consequence of the data.

Despite the promising results obtained in this study, there is a problem involving the lack of data beyond a certain redshift value. For some cases that involve the use of SDSS-BAO data, the center of the wavelet, determined by the parameter  $z^\dagger$ , is located near  $z \approx 2.4$ , and our data only reaches up to  $z = 2.34$ . Thus, there might be some features of the wavelets that simply cannot be constrained, such as the parameter  $\beta_h$ . To address this, our only recourse is to await the availability of more data beyond this range, at which point we can revisit and reperform the reconstructions done in this paper.

We conclude by recognizing that Hermitian wavelets, on top of the Hubble radius of the standard  $\Lambda$ CDM model, in the late Universe show a lot of promise in capturing the dynamics of deviations from the standard model of cosmology at the background level without altering the early Universe and the constraints on the matter density and the Hubble constant. These behaviors can then be attributed to underlying physics, such as a dynamical dark energy component, and different underlying physics with the same background phenomena can be tested at the perturbative level with full data.

## Appendix A: Additional Constraints and Figures

For completeness, we provide some results for the other reconstructed wavelets, although this might seem redundant given how similar they are. It is no surprise that most of the outcomes and behaviors reconstructed for  $\psi_1$  are shared by the rest of the Hermitian wavelets, given their similarities. This is easily verifiable by comparing Fig. 2 with Fig. A.1 and Fig. 3 with Fig. A.5. Despite using different Hermitian wavelets, the constraints on the parameter  $z^\dagger$  remain essentially the same, and the Hubble functions show only minor variations, primarily driven by the choice of datasets. Therefore, we have opted not to extend the discussion to the other wavelets.

A topic that requires some discussion is the result of the parameter inference procedure on the other two wavelet parameters,  $\alpha_h$  and  $\beta_h$ , found in Fig. A.2 and Fig. A.3, respectively. For  $\alpha_h$ , we observe a similar

behavior to the one displayed by  $z^\dagger$ , in the sense that the BAO dataset is the primary driver of the parameter inference, not **SN** or **PI**. We also observe bimodality in some cases and a lack of convergence in others. The parameter  $\beta_h$ , on the other hand, has very little impact on the datasets used. In Fig. A.3, it is evident that  $\beta_h$  remains largely unconstrained across most cases within the prior range considered. A few exceptions exist, where a faint maximum appears, such as in  $\psi_2$  or  $\psi_4$  with **SB+SN**. This lack of a well-defined posterior is expected for this particular parameter, given its minimal impact on the overall wavelet behavior (as shown in Fig. 1) and the limited data available beyond  $z \sim 2.3$ , as discussed in Section IV. While these parameters do play a role in shaping the wavelet, their overall impact is less significant than that of  $z^\dagger$ . Therefore, their discussion has been reserved for this appendix.

Finally, and to aid in the understanding and clarity of the results presented in this study with regards to the reconstructed  $H(z)/(1+z)$ , we include additional figures that provide enhanced visualizations of the wavelet behavior in the late Universe. These figures are artistically adapted versions of the previously shown plots in Fig. 3, designed to improve readability and facilitate a clearer interpretation of the data.

## ACKNOWLEDGEMENTS

L.A.E. was supported by CONAHCyT México. E.Ö. acknowledges support from the Türkiye Bilimsel ve Teknolojik Araştırma Kurumu (TÜBİTAK, Scientific and Technological Research Council of Turkey) through the 2214/A National Graduate Scholarship Program. Ö.A. acknowledges the support by the Turkish Academy of Sciences in scheme of the Outstanding Young Scientist Award (TÜBA-GEBİP). E.D.V. is supported by a Royal Society Dorothy Hodgkin Research Fellowship. J.A.V. acknowledges the support provided by FOSEC SEP-CONACYT Investigación Básica A1-S-21925, FORDECYT-PRONACES-CONACYT/304001/2020 and UNAM-DGAPA-PAPIIT IN117723. We also want to thank the Unidad de Cómputo of ICF-UNAM for their assistance in the maintenance and use of the computing equipment. This article is based upon work from COST Action CA21136 Addressing observational tensions in cosmology with systematics and fundamental physics (CosmoVerse) supported by COST (European Cooperation in Science and Technology).

---

[1] A. G. Riess *et al.* (Supernova Search Team), Observational evidence from supernovae for an accelerating uni-

verse and a cosmological constant, *Astron. J.* **116**, 1009 (1998), [astro-ph/9805201](#).

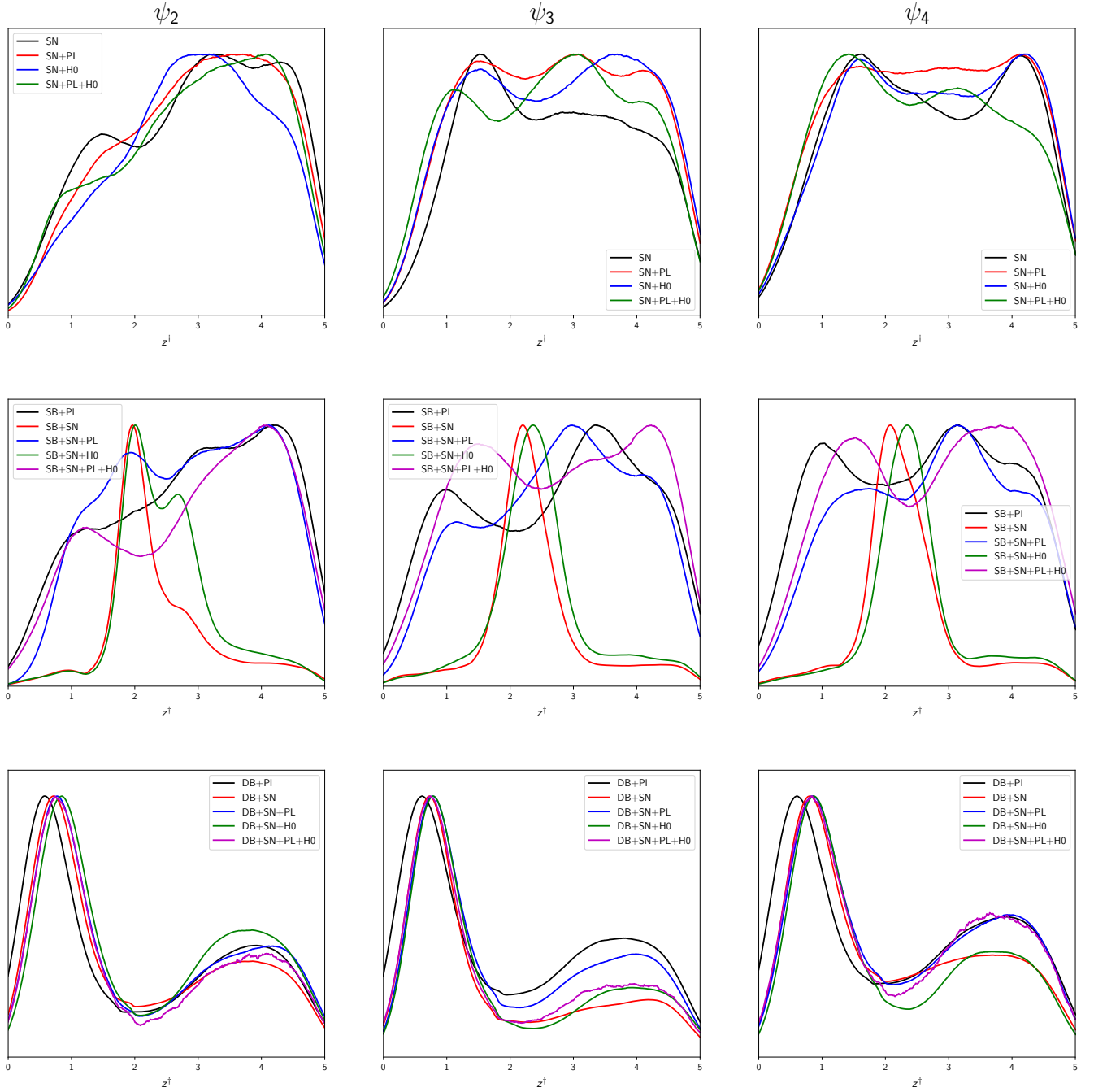


FIG. A.1: 1D marginalized posterior distributions for the reconstructed parameter  $z^\dagger$  for (from left to right)  $\psi_2(z)$ ,  $\psi_3(z)$ , and  $\psi_4(z)$ . We present the results in three different panels to illustrate the effect of the BAO datasets on the posteriors. These plots were created using the Python library `getdist` [202].

- [2] S. Perlmutter *et al.* (Supernova Cosmology Project), Measurements of  $\Omega$  and  $\Lambda$  from 42 high redshift supernovae, *Astrophys. J.* **517**, 565 (1999), [astro-ph/9812133](#).
- [3] R. Amanullah *et al.*, Spectra and Light Curves of Six Type Ia Supernovae at  $0.511 < z < 1.12$  and the Union2 Compilation, *Astrophys. J.* **716**, 712 (2010), [1004.1711](#).
- [4] S. Perlmutter *et al.* (Supernova Cosmology Project), Discovery of a supernova explosion at half the age of the Universe and its cosmological implications, *Nature* **391**, 51 (1998), [astro-ph/9712212](#).
- [5] R. Adam *et al.* (Planck), Planck 2015 results. I. Overview of products and scientific results, *Astron. Astrophys.* **594**, A1 (2016), [1502.01582](#).
- [6] C. L. Bennett *et al.* (WMAP), Nine-Year Wilkinson Microwave Anisotropy Probe (WMAP) Observations: Final Maps and Results, *Astrophys. J. Suppl.* **208**, 20 (2013), [1212.5225](#).

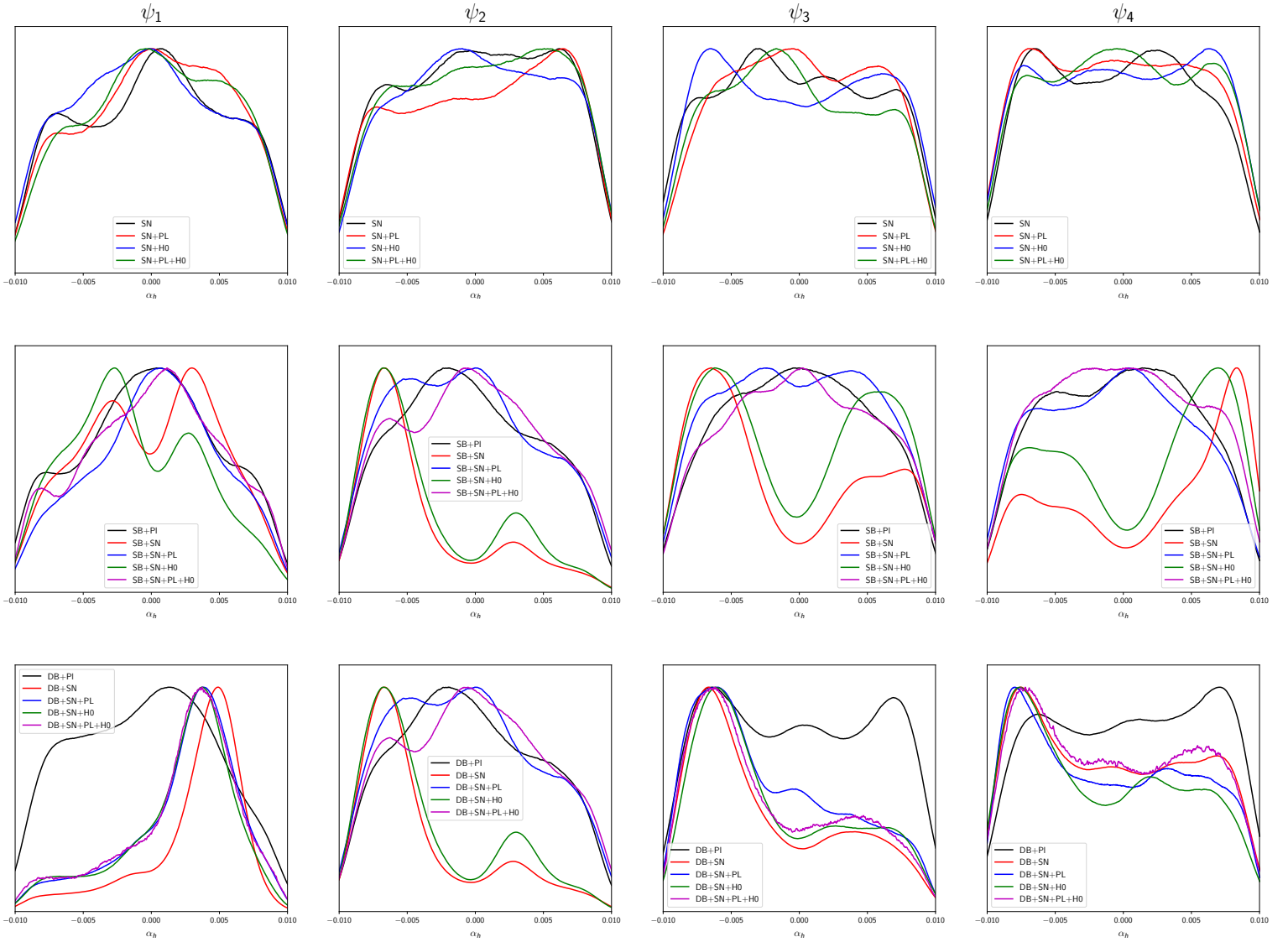


FIG. A.2: 1D marginalized posterior distributions for the reconstructed parameter  $\alpha_h$  for, from left to right,  $\psi_2(z)$ ,  $\psi_3(z)$ , and  $\psi_4(z)$ . We present the results in three different panels to illustrate the effect of the BAO datasets on the posteriors. These plots were created using the Python library `getdist` [202].

- [7] E. Komatsu *et al.* (WMAP), Seven-Year Wilkinson Microwave Anisotropy Probe (WMAP) Observations: Cosmological Interpretation, *Astrophys. J. Suppl.* **192**, 18 (2011), 1001.4538.
- [8] N. Aghanim *et al.* (Planck), Planck 2018 results. VI. Cosmological parameters, *Astron. Astrophys.* **641**, A6 (2020), [Erratum: *Astron. Astrophys.* 652, C4 (2021)], 1807.06209.
- [9] D. H. Weinberg, M. J. Mortonson, D. J. Eisenstein, C. Hirata, A. G. Riess, and E. Rozo, Observational Probes of Cosmic Acceleration, *Phys. Rept.* **530**, 87 (2013), 1201.2434.
- [10] M. Li, X.-D. Li, S. Wang, and Y. Wang, Dark Energy: A Brief Review, *Front. Phys. (Beijing)* **8**, 828 (2013), 1209.0922.
- [11] B. A. Reid *et al.*, Cosmological Constraints from the Clustering of the Sloan Digital Sky Survey DR7 Luminous Red Galaxies, *Mon. Not. Roy. Astron. Soc.* **404**, 60 (2010), 0907.1659.
- [12] W. J. Percival *et al.* (SDSS), Baryon Acoustic Oscillations in the Sloan Digital Sky Survey Data Release 7 Galaxy Sample, *Mon. Not. Roy. Astron. Soc.* **401**, 2148 (2010), 0907.1660.
- [13] K. N. Abazajian *et al.* (SDSS), The Seventh Data Release of the Sloan Digital Sky Survey, *Astrophys. J. Suppl.* **182**, 543 (2009), 0812.0649.
- [14] V. Mossa *et al.*, The baryon density of the Universe from an improved rate of deuterium burning, *Nature* **587**, 210 (2020).
- [15] S. Aiola *et al.* (ACT), The Atacama Cosmology Telescope: DR4 Maps and Cosmological Parameters, *JCAP* **12**, 047, 2007.07288.
- [16] S. Alam *et al.* (eBOSS), Completed SDSS-IV extended Baryon Oscillation Spectroscopic Survey: Cosmological

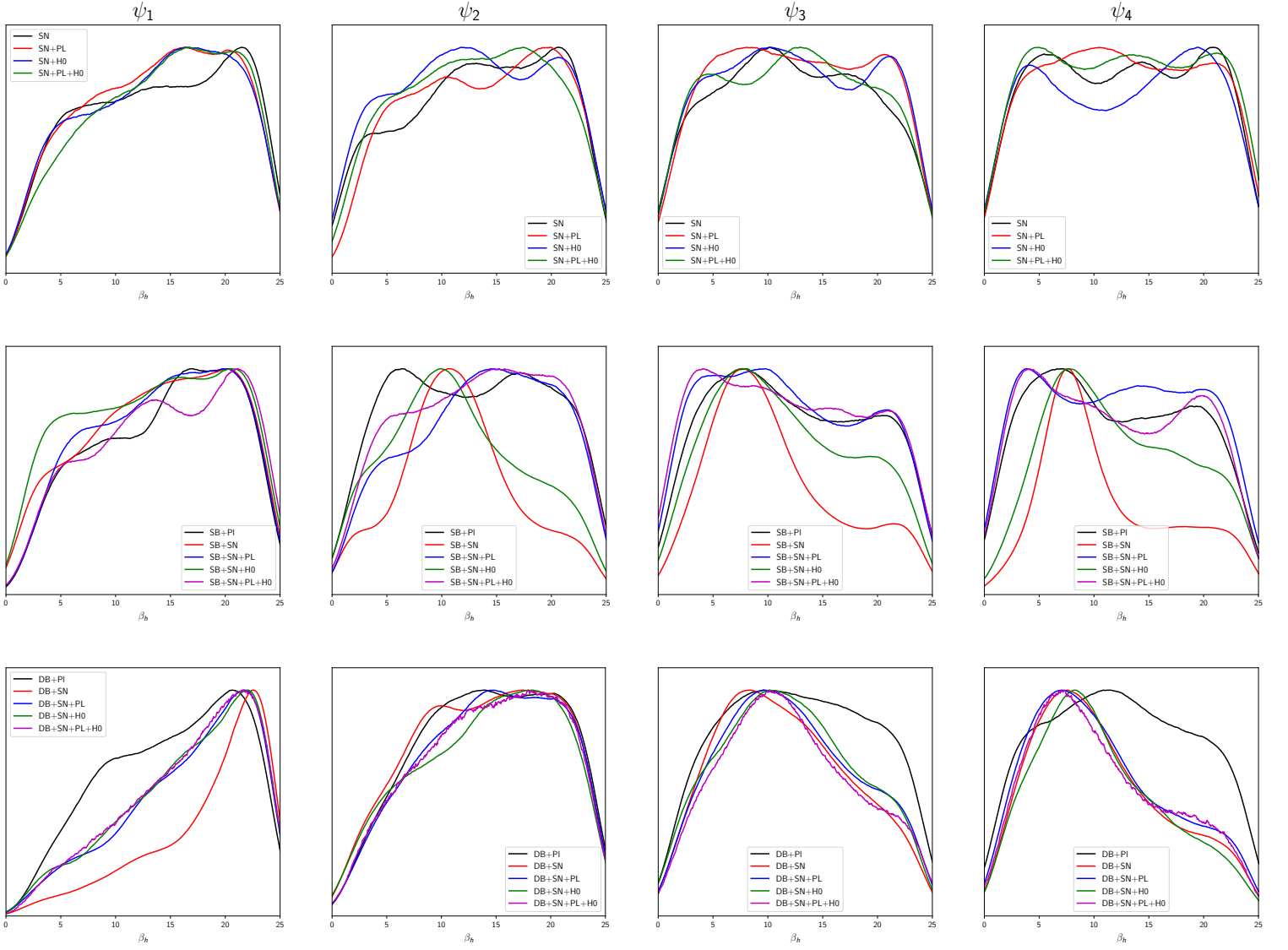


FIG. A.3: 1D marginalized posterior distributions for the reconstructed parameter  $\beta_h$  for, from left to right,  $\psi_1(z)$ ,  $\psi_2(z)$ ,  $\psi_3(z)$ , and  $\psi_4(z)$ . We present the results in three different panels to illustrate the effect of the BAO datasets on the posteriors. These plots were created using the Python library `getdist` [202].

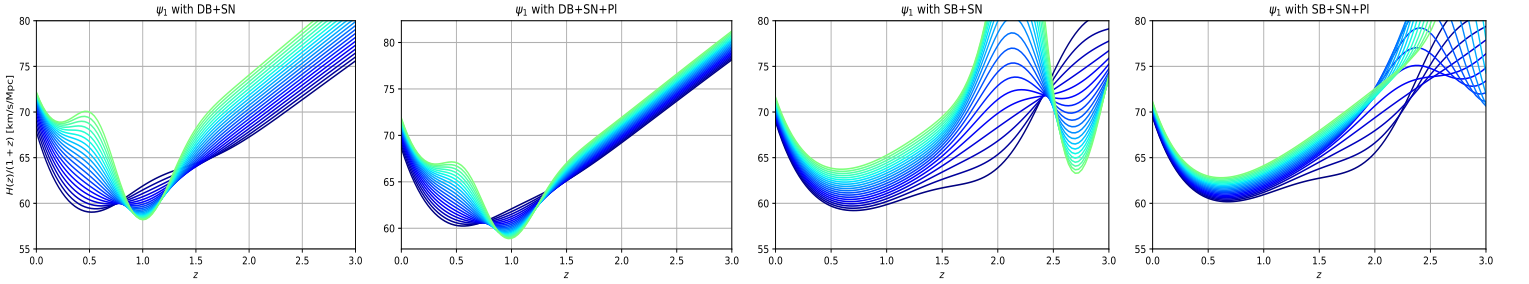


FIG. A.4: Artistically adapted version of Fig. 3 to enhance the readability of wavelet behavior in the late Universe.

implications from two decades of spectroscopic surveys at the Apache Point Observatory, *Phys. Rev. D* **103**, 083533 (2021), 2007.08991.

[17] L. Balkenhol *et al.* (SPT-3G), Measurement of the CMB temperature power spectrum and constraints on cosmology from the SPT-3G 2018 TT, TE, and EE dataset,

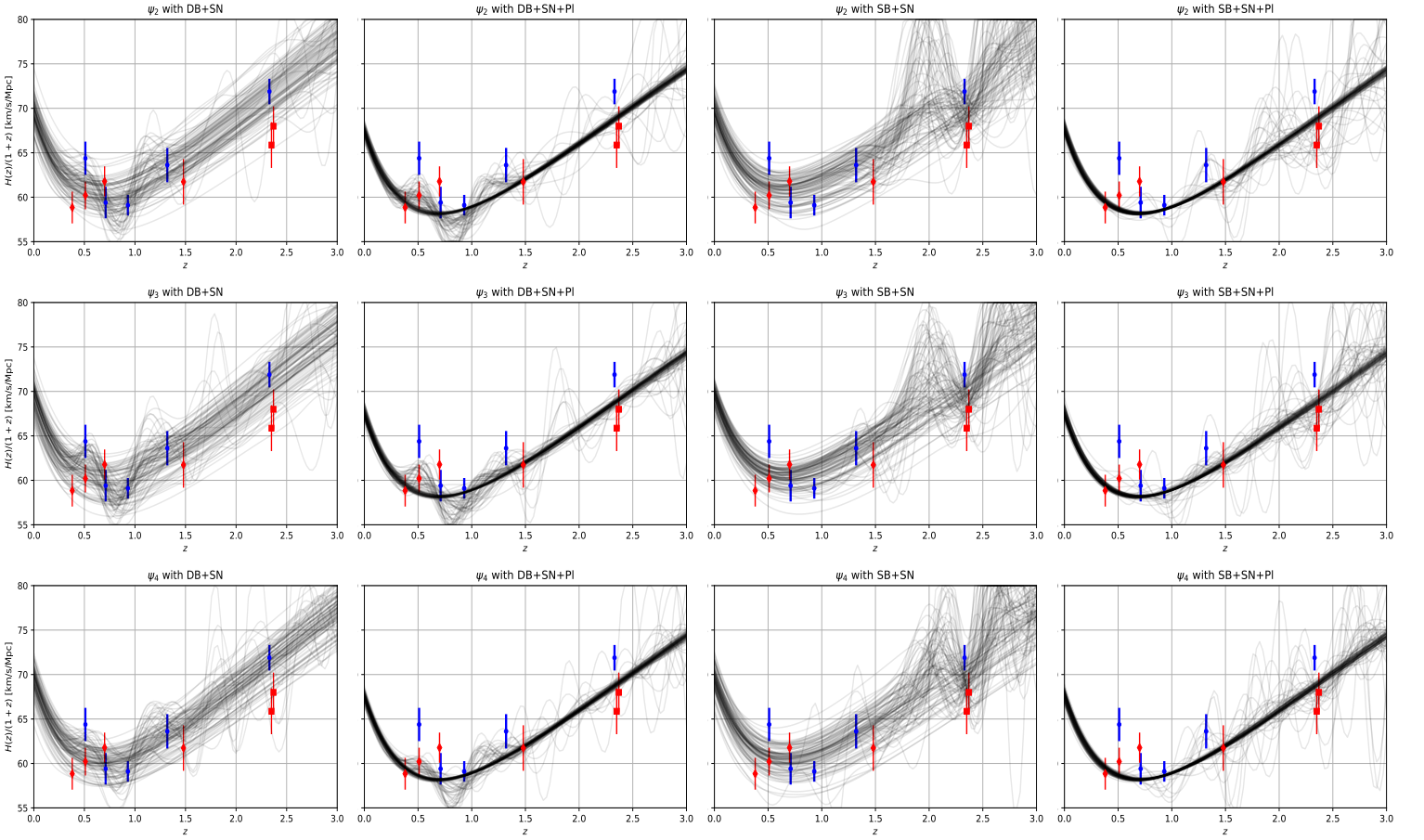


FIG. A.5: Functional posterior for  $H(z)/(1+z)$  for  $\psi_1(z)$  using four distinct data combinations: **DB+SN**, **DB+SN+PI**, **SB+SN**, and **SB+SN+PI**. The red (blue) error bars correspond to the SDSS (DESI) BAO distance  $D_H(z)/r_d$  measurements. The size of the sound horizon was fixed at the robust value of 147 Mpc to highlight the BAO data in the figure. The plots were created using the Python library `fgivenx` [203].

- [Phys. Rev. D \*\*108\*\*, 023510 \(2023\), 2212.05642.](#)
- [18] S. Weinberg, The Cosmological Constant Problem, [Rev. Mod. Phys. \*\*61\*\*, 1 \(1989\).](#)
- [19] V. Sahni, The Cosmological constant problem and quintessence, [Class. Quant. Grav. \*\*19\*\*, 3435 \(2002\), astro-ph/0202076.](#)
- [20] L.-M. Wang, R. R. Caldwell, J. P. Ostriker, and P. J. Steinhardt, Cosmic concordance and quintessence, [Astrophys. J. \*\*530\*\*, 17 \(2000\), astro-ph/9901388.](#)
- [21] V. Sahni, Dark matter and dark energy, [Lect. Notes Phys. \*\*653\*\*, 141 \(2004\), astro-ph/0403324.](#)
- [22] U. Alam, V. Sahni, and A. A. Starobinsky, The Case for dynamical dark energy revisited, [JCAP \*\*06\*\*, 008, astro-ph/0403687.](#)
- [23] P. Bull *et al.*, Beyond  $\Lambda$ CDM: Problems, solutions, and the road ahead, [Phys. Dark Univ. \*\*12\*\*, 56 \(2016\), 1512.05356.](#)
- [24] L. Verde, T. Treu, and A. G. Riess, Tensions between the Early and the Late Universe, [Nature Astron. \*\*3\*\*, 891 \(2019\), 1907.10625.](#)
- [25] E. Di Valentino *et al.*, Snowmass2021 - Letter of interest cosmology intertwined II: The hubble constant tension, [Astropart. Phys. \*\*131\*\*, 102605 \(2021\), 2008.11284.](#)
- [26] E. Di Valentino, O. Mena, S. Pan, L. Visinelli, W. Yang, A. Melchiorri, D. F. Mota, A. G. Riess, and J. Silk, In the realm of the Hubble tension—a review of solutions, [Class. Quant. Grav. \*\*38\*\*, 153001 \(2021\), 2103.01183.](#)
- [27] A. G. Riess *et al.*, A Comprehensive Measurement of the Local Value of the Hubble Constant with 1 km/s/Mpc Uncertainty from the Hubble Space Telescope and the SH0ES Team, [Astrophys. J. Lett. \*\*934\*\*, L7 \(2022\), 2112.04510.](#)
- [28] L. Knox and M. Millea, Hubble constant hunter’s guide, [Phys. Rev. D \*\*101\*\*, 043533 \(2020\), 1908.03663.](#)
- [29] M. Kamionkowski and A. G. Riess, The Hubble Tension and Early Dark Energy, [Ann. Rev. Nucl. Part. Sci. \*\*73\*\*, 153 \(2023\), 2211.04492.](#)
- [30] L. Verde, N. Schöneberg, and H. Gil-Marín, A tale of many  $H_0$ , (2023), [2311.13305.](#)
- [31] E. Di Valentino and D. Brout, eds., [The Hubble Constant Tension](#), Springer Series in Astrophysics and Cosmology (Springer, 2024).
- [32] L. Breuval, A. G. Riess, S. Casertano, W. Yuan, L. M. Macri, M. Romaniello, Y. S. Murakami, D. Scolnic, G. S. Anand, and I. Soszyński, Small Magellanic Cloud Cepheids Observed with the Hubble Space Telescope Provide a New Anchor for the SH0ES Distance Ladder,

- (2024), [2404.08038](#).
- [33] S. Li, A. G. Riess, S. Casertano, G. S. Anand, D. M. Scolnic, W. Yuan, L. Breuval, and C. D. Huang, Reconnaissance with JWST of the J-region Asymptotic Giant Branch in Distance Ladder Galaxies: From Irregular Luminosity Functions to Approximation of the Hubble Constant, *Astrophys. J.* **966**, 20 (2024), [2401.04777](#).
- [34] Y. S. Murakami, A. G. Riess, B. E. Stahl, W. D. Kenworthy, D.-M. A. Pluck, A. Macoreta, D. Brout, D. O. Jones, D. M. Scolnic, and A. V. Filippenko, Leveraging SN Ia spectroscopic similarity to improve the measurement of  $H_0$ , *JCAP* **11**, 046, [2306.00070](#).
- [35] L. Perivolaropoulos, Hubble Tension or Distance Ladder Crisis?, (2024), [2408.11031](#).
- [36] E. Di Valentino *et al.*, Cosmology intertwined III:  $f\sigma_8$  and  $S_8$ , *Astropart. Phys.* **131**, 102604 (2021), [2008.11285](#).
- [37] M. Douspis, L. Salvati, and N. Aghanim, On the Tension between Large Scale Structures and Cosmic Microwave Background, *PoS EDSU2018*, 037 (2018), [1901.05289](#).
- [38] T. M. C. Abbott *et al.* (DES), Dark Energy Survey Year 3 results: Cosmological constraints from galaxy clustering and weak lensing, *Phys. Rev. D* **105**, 023520 (2022), [2105.13549](#).
- [39] E. Di Valentino and S. Bridle, Exploring the Tension between Current Cosmic Microwave Background and Cosmic Shear Data, *Symmetry* **10**, 585 (2018).
- [40] T. M. C. Abbott *et al.* (Kilo-Degree Survey, DES), DES Y3 + KiDS-1000: Consistent cosmology combining cosmic shear surveys, *Open J. Astrophys.* **6**, 2305.17173 (2023), [2305.17173](#).
- [41] T. Tröster *et al.*, Cosmology from large-scale structure: Constraining  $\Lambda$ CDM with BOSS, *Astron. Astrophys.* **633**, L10 (2020), [1909.11006](#).
- [42] C. Heymans *et al.*, KiDS-1000 Cosmology: Multi-probe weak gravitational lensing and spectroscopic galaxy clustering constraints, *Astron. Astrophys.* **646**, A140 (2021), [2007.15632](#).
- [43] R. Dalal *et al.*, Hyper Suprime-Cam Year 3 results: Cosmology from cosmic shear power spectra, *Phys. Rev. D* **108**, 123519 (2023), [2304.00701](#).
- [44] S. Chen *et al.*, Not all lensing is low: An analysis of DESI $\times$ DES using the Lagrangian Effective Theory of LSS, (2024), [2407.04795](#).
- [45] J. Kim *et al.* (ACT, DESI), The Atacama Cosmology Telescope DR6 and DESI: Structure formation over cosmic time with a measurement of the cross-correlation of CMB Lensing and Luminous Red Galaxies, (2024), [2407.04606](#).
- [46] L. Faga *et al.* (DES), Dark Energy Survey Year 3 Results: Cosmology from galaxy clustering and galaxy-galaxy lensing in harmonic space, (2024), [2406.12675](#).
- [47] J. Harnois-Deraps *et al.*, KiDS-1000 and DES-Y1 combined: Cosmology from peak count statistics, (2024), [2405.10312](#).
- [48] A. Dvornik *et al.*, KiDS-1000: Combined halo-model cosmology constraints from galaxy abundance, galaxy clustering and galaxy-galaxy lensing, *Astron. Astrophys.* **675**, A189 (2023), [2210.03110](#).
- [49] S. A. Adil, O. Akarsu, M. Malekjani, E. O. Colgáin, S. Pourojaghi, A. A. Sen, and M. M. Sheikh-Jabbari,  $S_8$  increases with effective redshift in  $\Lambda$ CDM cosmology, *Mon. Not. Roy. Astron. Soc.* **528**, L20 (2023), [2303.06928](#).
- [50] E. Abdalla *et al.*, Cosmology intertwined: A review of the particle physics, astrophysics, and cosmology associated with the cosmological tensions and anomalies, *JHEAp* **34**, 49 (2022), [2203.06142](#).
- [51] L. Perivolaropoulos and F. Skara, Challenges for  $\Lambda$ CDM: An update, *New Astron. Rev.* **95**, 101659 (2022), [2105.05208](#).
- [52] E. Di Valentino, Challenges of the Standard Cosmological Model, *Universe* **8**, 399 (2022).
- [53] R. Murgia, S. Gariazzo, and N. Fornengo, Constraints on the Coupling between Dark Energy and Dark Matter from CMB data, *JCAP* **04**, 014, [1602.01765](#).
- [54] A. Pourtsidou and T. Tram, Reconciling CMB and structure growth measurements with dark energy interactions, *Phys. Rev. D* **94**, 043518 (2016), [1604.04222](#).
- [55] R. C. Nunes, S. Pan, and E. N. Saridakis, New constraints on interacting dark energy from cosmic chronometers, *Phys. Rev. D* **94**, 023508 (2016), [1605.01712](#).
- [56] E. Di Valentino, A. Melchiorri, and J. Silk, Reconciling Planck with the local value of  $H_0$  in extended parameter space, *Phys. Lett. B* **761**, 242 (2016), [1606.00634](#).
- [57] S. Kumar and R. C. Nunes, Probing the interaction between dark matter and dark energy in the presence of massive neutrinos, *Phys. Rev. D* **94**, 123511 (2016), [1608.02454](#).
- [58] S. Kumar and R. C. Nunes, Echo of interactions in the dark sector, *Phys. Rev. D* **96**, 103511 (2017), [1702.02143](#).
- [59] E. Di Valentino, A. Melchiorri, and O. Mena, Can interacting dark energy solve the  $H_0$  tension?, *Phys. Rev. D* **96**, 043503 (2017), [1704.08342](#).
- [60] E. Di Valentino, Crack in the cosmological paradigm, *Nature Astron.* **1**, 569 (2017), [1709.04046](#).
- [61] E. Di Valentino, E. V. Linder, and A. Melchiorri, Vacuum phase transition solves the  $H_0$  tension, *Phys. Rev. D* **97**, 043528 (2018), [1710.02153](#).
- [62] E. Di Valentino, C. Bøehm, E. Hivon, and F. R. Bouchet, Reducing the  $H_0$  and  $\sigma_8$  tensions with Dark Matter-neutrino interactions, *Phys. Rev. D* **97**, 043513 (2018), [1710.02559](#).
- [63] K. Dutta, Ruchika, A. Roy, A. A. Sen, and M. M. Sheikh-Jabbari, Beyond  $\Lambda$ CDM with low and high redshift data: implications for dark energy, *Gen. Rel. Grav.* **52**, 15 (2020), [1808.06623](#).
- [64] W. Yang, A. Mukherjee, E. Di Valentino, and S. Pan, Interacting dark energy with time varying equation of state and the  $H_0$  tension, *Phys. Rev. D* **98**, 123527 (2018), [1809.06883](#).
- [65] V. Poulin, T. L. Smith, T. Karwal, and M. Kamionkowski, Early Dark Energy Can Resolve The Hubble Tension, *Phys. Rev. Lett.* **122**, 221301 (2019), [1811.04083](#).
- [66] E. Di Valentino, R. Z. Ferreira, L. Visinelli, and U. Danielsson, Late time transitions in the quintessence field and the  $H_0$  tension, *Phys. Dark Univ.* **26**, 100385 (2019), [1906.11255](#).
- [67] L. Visinelli, S. Vagnozzi, and U. Danielsson, Revisiting a negative cosmological constant from low-redshift data, *Symmetry* **11**, 1035 (2019), [1907.07953](#).
- [68] S. Pan, W. Yang, E. Di Valentino, A. Shafieloo, and S. Chakraborty, Reconciling  $H_0$  tension in a six parameter space?, *JCAP* **06** (06), 062, [1907.12551](#).

- [69] E. Di Valentino, A. Melchiorri, O. Mena, and S. Vagnozzi, Interacting dark energy in the early 2020s: A promising solution to the  $H_0$  and cosmic shear tensions, *Phys. Dark Univ.* **30**, 100666 (2020), 1908.04281.
- [70] T. L. Smith, V. Poulin, and M. A. Amin, Oscillating scalar fields and the Hubble tension: a resolution with novel signatures, *Phys. Rev. D* **101**, 063523 (2020), 1908.06995.
- [71] F. Niedermann and M. S. Sloth, New early dark energy, *Phys. Rev. D* **103**, L041303 (2021), 1910.10739.
- [72] R. von Marttens, L. Lombriser, M. Kunz, V. Marra, L. Casarini, and J. Alcaniz, Dark degeneracy I: Dynamical or interacting dark energy?, *Phys. Dark Univ.* **28**, 100490 (2020), 1911.02618.
- [73] O. Akarsu, J. D. Barrow, L. A. Escamilla, and J. A. Vazquez, Graduated dark energy: Observational hints of a spontaneous sign switch in the cosmological constant, *Phys. Rev. D* **101**, 063528 (2020), 1912.08751.
- [74] G. Ye and Y.-S. Piao, Is the Hubble tension a hint of AdS phase around recombination?, *Phys. Rev. D* **101**, 083507 (2020), 2001.02451.
- [75] W. Yang, E. Di Valentino, S. Pan, S. Basilakos, and A. Paliathanasis, Metastable dark energy models in light of *Planck* 2018 data: Alleviating the  $H_0$  tension, *Phys. Rev. D* **102**, 063503 (2020), 2001.04307.
- [76] W. Yang, E. Di Valentino, O. Mena, S. Pan, and R. C. Nunes, All-inclusive interacting dark sector cosmologies, *Phys. Rev. D* **101**, 083509 (2020), 2001.10852.
- [77] C. Krishnan, E. O. Colgáin, Ruchika, A. A. Sen, M. M. Sheikh-Jabbari, and T. Yang, Is there an early Universe solution to Hubble tension?, *Phys. Rev. D* **102**, 103525 (2020), 2002.06044.
- [78] M. Lucca and D. C. Hooper, Shedding light on dark matter-dark energy interactions, *Phys. Rev. D* **102**, 123502 (2020), 2002.06127.
- [79] E. Di Valentino, A. Mukherjee, and A. A. Sen, Dark Energy with Phantom Crossing and the  $H_0$  Tension, *Entropy* **23**, 404 (2021), 2005.12587.
- [80] R. Calderón, R. Gannouji, B. L’Huillier, and D. Polarski, Negative cosmological constant in the dark sector?, *Phys. Rev. D* **103**, 023526 (2021), 2008.10237.
- [81] E. Di Valentino and O. Mena, A fake Interacting Dark Energy detection?, *Mon. Not. Roy. Astron. Soc.* **500**, L22 (2020), 2009.12620.
- [82] E. Di Valentino, A combined analysis of the  $H_0$  late time direct measurements and the impact on the Dark Energy sector, *Mon. Not. Roy. Astron. Soc.* **502**, 2065 (2021), 2011.00246.
- [83] W. Yang, E. Di Valentino, S. Pan, Y. Wu, and J. Lu, Dynamical dark energy after Planck CMB final release and  $H_0$  tension, *Mon. Not. Roy. Astron. Soc.* **501**, 5845 (2021), 2101.02168.
- [84] S. Kumar, Remedy of some cosmological tensions via effective phantom-like behavior of interacting vacuum energy, *Phys. Dark Univ.* **33**, 100862 (2021), 2102.12902.
- [85] W. Yang, E. Di Valentino, S. Pan, A. Shafieloo, and X. Li, Generalized emergent dark energy model and the Hubble constant tension, *Phys. Rev. D* **104**, 063521 (2021), 2103.03815.
- [86] R. C. Nunes and E. Di Valentino, Dark sector interaction and the supernova absolute magnitude tension, *Phys. Rev. D* **104**, 063529 (2021), 2107.09151.
- [87] N. Schöneberg, G. Franco Abellán, A. Pérez Sánchez, S. J. Witte, V. Poulin, and J. Lesgourgues, The H0 Olympics: A fair ranking of proposed models, *Phys. Rept.* **984**, 1 (2022), 2107.10291.
- [88] G. Ye, J. Zhang, and Y.-S. Piao, Alleviating both H0 and S8 tensions: Early dark energy lifts the CMB-lockdown on ultralight axion, *Phys. Lett. B* **839**, 137770 (2023), 2107.13391.
- [89] O. Akarsu, S. Kumar, E. Özülker, and J. A. Vazquez, Relaxing cosmological tensions with a sign switching cosmological constant, *Phys. Rev. D* **104**, 123512 (2021), 2108.09239.
- [90] V. Poulin, T. L. Smith, and A. Bartlett, Dark energy at early times and ACT data: A larger Hubble constant without late-time priors, *Phys. Rev. D* **104**, 123550 (2021), 2109.06229.
- [91] E. Di Valentino, S. Gariazzo, C. Giunti, O. Mena, S. Pan, and W. Yang, Minimal dark energy: Key to sterile neutrino and Hubble constant tensions?, *Phys. Rev. D* **105**, 103511 (2022), 2110.03990.
- [92] G. Alestas, D. Camarena, E. Di Valentino, L. Kazantzidis, V. Marra, S. Nesseris, and L. Perivolaropoulos, Late-transition versus smooth  $H(z)$ -deformation models for the resolution of the Hubble crisis, *Phys. Rev. D* **105**, 063538 (2022), 2110.04336.
- [93] S. Gariazzo, E. Di Valentino, O. Mena, and R. C. Nunes, Late-time interacting cosmologies and the Hubble constant tension, *Phys. Rev. D* **106**, 023530 (2022), 2111.03152.
- [94] F. Niedermann and M. S. Sloth, Hot new early dark energy, *Phys. Rev. D* **105**, 063509 (2022), 2112.00770.
- [95] A. A. Sen, S. A. Adil, and S. Sen, Do cosmological observations allow a negative  $\Lambda$ ?, *Mon. Not. Roy. Astron. Soc.* **518**, 1098 (2022), 2112.10641.
- [96] L. Heisenberg, H. Villarrubia-Rojo, and J. Zosso, Simultaneously solving the H0 and  $\sigma_8$  tensions with late dark energy, *Phys. Dark Univ.* **39**, 101163 (2023), 2201.11623.
- [97] L. A. Anchordoqui, V. Barger, D. Marfatia, and J. F. Soriano, Decay of multiple dark matter particles to dark radiation in different epochs does not alleviate the Hubble tension, *Phys. Rev. D* **105**, 103512 (2022), 2203.04818.
- [98] S. Di Gennaro and Y. C. Ong, Sign Switching Dark Energy from a Running Barrow Entropy, *Universe* **8**, 541 (2022), 2205.09311.
- [99] O. Akarsu, S. Kumar, E. Özülker, J. A. Vazquez, and A. Yadav, Relaxing cosmological tensions with a sign switching cosmological constant: Improved results with Planck, BAO, and Pantheon data, *Phys. Rev. D* **108**, 023513 (2023), 2211.05742.
- [100] Y. C. Ong, An Effective Sign Switching Dark Energy: Lotka–Volterra Model of Two Interacting Fluids, *Universe* **9**, 437 (2023), 2212.04429.
- [101] N. Lee, Y. Ali-Haïmoud, N. Schöneberg, and V. Poulin, What It Takes to Solve the Hubble Tension through Modifications of Cosmological Recombination, *Phys. Rev. Lett.* **130**, 161003 (2023), 2212.04494.
- [102] A. Bernui, E. Di Valentino, W. Giarè, S. Kumar, and R. C. Nunes, Exploring the H0 tension and the evidence for dark sector interactions from 2D BAO measurements, *Phys. Rev. D* **107**, 103531 (2023), 2301.06097.
- [103] K. R. Mishra, S. K. J. Pacif, R. Kumar, and K. Bamba, Cosmological implications of an interacting model of



- dark matter & dark energy, *Phys. Dark Univ.* **40**, 101211 (2023), 2301.08743.
- [104] Y. Tiwari, B. Ghosh, and R. K. Jain, Towards a possible solution to the Hubble tension with Horndeski gravity, *Eur. Phys. J. C* **84**, 220 (2024), 2301.09382.
- [105] D. H. F. de Souza and R. Rosenfeld, Can neutrino-assisted early dark energy models ameliorate the  $H_0$  tension in a natural way?, *Phys. Rev. D* **108**, 083512 (2023), 2302.04644.
- [106] V. Poulin, T. L. Smith, and T. Karwal, The Ups and Downs of Early Dark Energy solutions to the Hubble tension: A review of models, hints and constraints circa 2023, *Phys. Dark Univ.* **42**, 101348 (2023), 2302.09032.
- [107] M. A. van der Westhuizen and A. Abebe, Interacting dark energy: clarifying the cosmological implications and viability conditions, *JCAP* **01**, 048, 2302.11949.
- [108] Y. Zhai, W. Giarè, C. van de Bruck, E. Di Valentino, O. Mena, and R. C. Nunes, A consistent view of interacting dark energy from multiple CMB probes, *JCAP* **07**, 032, 2303.08201.
- [109] J. S. Cruz, F. Niedermann, and M. S. Sloth, Cold New Early Dark Energy pulls the trigger on the  $H_0$  and  $S_8$  tensions: a simultaneous solution to both tensions without new ingredients, *JCAP* **11**, 033, 2305.08895.
- [110] W. Giarè, CMB Anomalies and the Hubble Tension, (2023), 2305.16919.
- [111] Ruchika, H. Rathore, S. Roy Choudhury, and V. Rentala, A gravitational constant transition within cepheids as supernovae calibrators can solve the Hubble tension, *JCAP* **06**, 056, 2306.05450.
- [112] K. L. Greene and F.-Y. Cyr-Racine, Thomson scattering: one rate to rule them all, *JCAP* **10**, 065, 2306.06165.
- [113] S. A. Adil, O. Akarsu, E. Di Valentino, R. C. Nunes, E. Özülker, A. A. Sen, and E. Specogna, Omnipotent dark energy: A phenomenological answer to the Hubble tension, *Phys. Rev. D* **109**, 023527 (2024), 2306.08046.
- [114] F. Niedermann and M. S. Sloth, New Early Dark Energy as a solution to the  $H_0$  and  $S_8$  tensions **3** (2023), 2307.03481.
- [115] E. Frion, D. Camarena, L. Giani, T. Miranda, D. Bertacca, V. Marra, and O. F. Piattella, Bayesian analysis of a Unified Dark Matter model with transition: can it alleviate the  $H_0$  tension? 10.21105/astro.2307.06320 (2023), 2307.06320.
- [116] G. Liu, Z. Zhou, Y. Mu, and L. Xu, Alleviating cosmological tensions with a coupled scalar fields model, *Phys. Rev. D* **108**, 083523 (2023), 2307.07228.
- [117] O. Akarsu, E. Di Valentino, S. Kumar, R. C. Nunes, J. A. Vazquez, and A. Yadav,  $\Lambda_s$ CDM model: A promising scenario for alleviation of cosmological tensions, (2023), 2307.10899.
- [118] G. A. Hoerning, R. G. Landim, L. O. Ponte, R. P. Rolim, F. B. Abdalla, and E. Abdalla, Constraints on interacting dark energy revisited: implications for the Hubble tension, (2023), 2308.05807.
- [119] S. Vagnozzi, Seven Hints That Early-Time New Physics Alone Is Not Sufficient to Solve the Hubble Tension, *Universe* **9**, 393 (2023), 2308.16628.
- [120] M. Höggås and E. Mörtzell, Hubble tension and fifth forces, *Phys. Rev. D* **108**, 124050 (2023), 2309.01744.
- [121] A. Gómez-Valent, A. Favale, M. Migliaccio, and A. A. Sen, Late-time phenomenology required to solve the  $H_0$  tension in view of the cosmic ladders and the anisotropic and angular BAO datasets, *Phys. Rev. D* **109**, 023525 (2024), 2309.07795.
- [122] A. Lapi, L. Boco, M. M. Cueli, B. S. Haridasu, T. Ronconi, C. Baccigalupi, and L. Danese, Little Ado about Everything:  $\eta$ CDM, a Cosmological Model with Fluctuation-driven Acceleration at Late Times, *Astrophys. J.* **959**, 83 (2023), 2310.06028.
- [123] S. Pan and W. Yang, On the interacting dark energy scenarios – the case for Hubble constant tension, (2023), 2310.07260.
- [124] G. Efstathiou, E. Rosenberg, and V. Poulin, Improved Planck Constraints on Axionlike Early Dark Energy as a Resolution of the Hubble Tension, *Phys. Rev. Lett.* **132**, 221002 (2024), 2311.00524.
- [125] R. Y. Wen, L. T. Hergt, N. Afshordi, and D. Scott, A cosmic glitch in gravity, *JCAP* **03**, 045, 2311.03028.
- [126] J. L. Cervantes-Cota, S. Galindo-Uribarri, and G. F. Smoot, The Unsettled Number: Hubble’s Tension, *Universe* **9**, 501 (2023), 2311.07552.
- [127] S. Castello, M. Mancarella, N. Grimm, D. Sobral-Blanco, I. Tutusaus, and C. Bonvin, Gravitational redshift constraints on the effective theory of interacting dark energy, *JCAP* **05**, 003, 2311.14425.
- [128] M. Forconi, W. Giarè, O. Mena, Ruchika, E. Di Valentino, A. Melchiorri, and R. C. Nunes, A double take on early and interacting dark energy from JWST, *JCAP* **05**, 097, 2312.11074.
- [129] L. A. Anchordoqui, I. Antoniadis, and D. Lust, Anti-de Sitter  $\rightarrow$  de Sitter transition driven by Casimir forces and mitigating tensions in cosmological parameters, *Phys. Lett. B* **855**, 138775 (2024), 2312.12352.
- [130] C. Pitrou and J.-P. Uzan, Hubble Tension as a Window on the Gravitation of the Dark Matter Sector, *Phys. Rev. Lett.* **132**, 191001 (2024), 2312.12493.
- [131] S. Pan, O. Seto, T. Takahashi, and Y. Toda, Constraints on sterile neutrinos and the cosmological tensions, (2023), 2312.15435.
- [132] Y.-H. Yao and X.-H. Meng, Can interacting dark energy with dynamical coupling resolve the Hubble tension, *Phys. Dark Univ.* **39**, 101165 (2023).
- [133] O. Akarsu, E. O. Colgáin, A. A. Sen, and M. M. Sheikh-Jabbari,  $\Lambda$ CDM Tensions: Localising Missing Physics through Consistency Checks, *Universe* **10**, 305 (2024), 2402.04767.
- [134] O. Akarsu, A. De Felice, E. Di Valentino, S. Kumar, R. C. Nunes, E. Ozulker, J. A. Vazquez, and A. Yadav,  $\Lambda_s$ CDM cosmology from a type-II minimally modified gravity, (2024), 2402.07716.
- [135] G. Garcia-Arroyo, L. A. Ureña López, and J. A. Vázquez, Interacting scalar fields: Dark matter and early dark energy, *Phys. Rev. D* **110**, 023529 (2024), 2402.08815.
- [136] D. Benisty, S. Pan, D. Staicova, E. Di Valentino, and R. C. Nunes, Late-Time constraints on Interacting Dark Energy: Analysis independent of  $H_0$ ,  $r_d$  and  $M_B$ , *Astron. Astrophys.* **688**, A156 (2024), 2403.00056.
- [137] S. Halder, J. de Haro, T. Saha, and S. Pan, Phase space analysis of sign-shifting interacting dark energy models, *Phys. Rev. D* **109**, 083522 (2024), 2403.01397.
- [138] K. Greene and F.-Y. Cyr-Racine, A Ratio-Preserving Approach to Cosmological Concordance, (2024), 2403.05619.

- [139] A. Krolewski, W. J. Percival, and A. Woodfinden, A new method to determine  $H_0$  from cosmological energy-density measurements, (2024), [2403.19227](#).
- [140] E. Silva, U. Zúñiga Bolaño, R. C. Nunes, and E. Di Valentino, Non-Linear Matter Power Spectrum Modeling in Interacting Dark Energy Cosmologies, (2024), [2403.19590](#).
- [141] W. Giarè, Y. Zhai, S. Pan, E. Di Valentino, R. C. Nunes, and C. van de Bruck, Tightening the reins on non-minimal dark sector physics: Interacting Dark Energy with dynamical and non-dynamical equation of state, (2024), [2404.02110](#).
- [142] M. Garny, F. Niedermann, H. Rubira, and M. S. Sloth, Hot new early dark energy bridging cosmic gaps: Supercooled phase transition reconciles stepped dark radiation solutions to the Hubble tension with BBN, *Phys. Rev. D* **110**, 023531 (2024), [2404.07256](#).
- [143] W. Giarè, Inflation, the Hubble tension, and early dark energy: An alternative overview, *Phys. Rev. D* **109**, 123545 (2024), [2404.12779](#).
- [144] G. Montani, N. Carlevaro, L. A. Escamilla, and E. Di Valentino, Kinetic Model for Dark Energy – Dark Matter Interaction: Scenario for the Hubble Tension, (2024), [2404.15977](#).
- [145] I. J. Allali, D. Aloni, and N. Schöneberg, Cosmological probes of Dark Radiation from Neutrino Mixing, (2024), [2404.16822](#).
- [146] L. A. Anchordoqui, I. Antoniadis, D. Lust, N. T. Noble, and J. F. Soriano, From infinite to infinitesimal: Using the Universe as a dataset to probe Casimir corrections to the vacuum energy from fields inhabiting the dark dimension, (2024), [2404.17334](#).
- [147] D. Bousis and L. Perivolaropoulos, Hubble tension tomography: BAO vs S<sub>n</sub>la distance tension, (2024), [2405.07039](#).
- [148] M. Baryakhtar, O. Simon, and Z. J. Weiner, Varying-constant cosmology from hyperlight, coupled scalars, (2024), [2405.10358](#).
- [149] O. Seto and Y. Toda, DESI constraints on varying electron mass model and axion-like early dark energy, (2024), [2405.11869](#).
- [150] R. T. Co, N. Fernandez, A. Ghalsasi, K. Harigaya, and J. Shelton, Axion baryogenesis puts a new spin on the Hubble tension, (2024), [2405.12268](#).
- [151] J. E. Gonzalez, M. Ferreira, L. R. Colaço, R. F. L. Holanda, and R. C. Nunes, Unveiling the Hubble Constant through Galaxy Cluster Gas Mass Fractions, (2024), [2405.13665](#).
- [152] H. Bagherian, M. Joseph, M. Schmaltz, and E. N. Sivarajan, Stepping into the Forest: Confronting Interacting Radiation Models for the Hubble Tension with Lyman- $\alpha$  Data, (2024), [2405.17554](#).
- [153] W. Giarè, J. Betts, C. van de Bruck, and E. Di Valentino, A model-independent test of pre-recombination New Physics: Machine Learning based estimate of the Sound Horizon from Gravitational Wave Standard Sirens and the Baryon Acoustic Oscillation Angular Scale, (2024), [2406.07493](#).
- [154] O. Akarsu, A. De Felice, E. Di Valentino, S. Kumar, R. C. Nunes, E. Ozulker, J. A. Vazquez, and A. Yadav, Cosmological constraints on  $\Lambda_s$ CDM scenario in a type II minimally modified gravity, (2024), [2406.07526](#).
- [155] G. P. Lynch, L. Knox, and J. Chluba, DESI and the Hubble tension in light of modified recombination, (2024), [2406.10202](#).
- [156] A. Yadav, S. Kumar, C. Kibris, and O. Akarsu,  $\Lambda_s$ CDM cosmology: Alleviating major cosmological tensions by predicting standard neutrino properties, (2024), [2406.18496](#).
- [157] A. Aboubrahim and P. Nath, Interacting ultralight dark matter and dark energy and fits to cosmological data in a field theory approach, (2024), [2406.19284](#).
- [158] Y. Toda, W. Giarè, E. Özulker, E. Di Valentino, and S. Vagnozzi, Combining pre- and post-recombination new physics to address cosmological tensions: case study with varying electron mass and a sign-switching cosmological constant, (2024), [2407.01173](#).
- [159] N. N. Pooya, Growth of matter perturbations in the interacting dark energy-dark matter scenarios, *Phys. Rev. D* **110**, 043510 (2024), [2407.03766](#).
- [160] S. Dwivedi and M. Höggås, 2D BAO vs 3D BAO: solving the Hubble tension with alternative cosmological models, (2024), [2407.04322](#).
- [161] X. Tang, Y.-Z. Ma, W.-M. Dai, and H.-J. He, Constraining holographic dark energy and analyzing cosmological tensions, *Phys. Dark Univ.* **46**, 101568 (2024), [2407.08427](#).
- [162] T.-N. Li, P.-J. Wu, G.-H. Du, S.-J. Jin, H.-L. Li, J.-F. Zhang, and X. Zhang, Constraints on interacting dark energy models from the DESI BAO and DES supernovae data, (2024), [2407.14934](#).
- [163] N. Schöneberg and L. Vacher, The mass effect – Variations of masses and their impact on cosmology, (2024), [2407.16845](#).
- [164] V. Poulin, T. L. Smith, R. Calderón, and T. Simon, On the implications of the ‘cosmic calibration tension’ beyond  $H_0$  and the synergy between early- and late-time new physics, (2024), [2407.18292](#).
- [165] J.-Q. Jiang, D. Pedrotti, S. S. da Costa, and S. Vagnozzi, Non-parametric late-time expansion history reconstruction and implications for the Hubble tension in light of DESI, (2024), [2408.02365](#).
- [166] Ruchika, L. Perivolaropoulos, and A. Melchiorri, Effects of a local physics change on the SH0ES determination of  $H_0$ , (2024), [2408.03875](#).
- [167] D. Pedrotti, J.-Q. Jiang, L. A. Escamilla, S. S. da Costa, and S. Vagnozzi, Multidimensionality of the Hubble tension: the roles of  $\Omega_m$  and  $\omega_c$ , (2024), [2408.04530](#).
- [168] J. Kochappan, Lu-Yin, B.-H. Lee, and T. Ghosh, Observational evidence for Early Dark Energy as a unified explanation for Cosmic Birefringence and the Hubble tension, (2024), [2408.09521](#).
- [169] M. T. Manoharan, Insights on Granda–Oliveros holographic dark energy: possibility of negative dark energy at  $z \gtrsim 2$ , *Eur. Phys. J. C* **84**, 552 (2024).
- [170] E. Aubourg *et al.* (BOSS), Cosmological implications of baryon acoustic oscillation measurements, *Phys. Rev. D* **92**, 123516 (2015), [1411.1074](#).
- [171] Y. Wang, L. Pogosian, G.-B. Zhao, and A. Zucca, Evolution of dark energy reconstructed from the latest observations, *Astrophys. J. Lett.* **869**, L8 (2018), [1807.03772](#).
- [172] V. Poulin, K. K. Boddy, S. Bird, and M. Kamionkowski, Implications of an extended dark energy cosmology with massive neutrinos for cosmological tensions, *Phys. Rev. D* **97**, 123504 (2018), [1803.02474](#).
- [173] D. Tamayo and J. A. Vazquez, Fourier-series expansion of the dark-energy equation of state, *Mon. Not. Roy.*

- Astron. Soc.* **487**, 729 (2019), 1901.08679.
- [174] A. Bonilla, S. Kumar, and R. C. Nunes, Measurements of  $H_0$  and reconstruction of the dark energy properties from a model-independent joint analysis, *Eur. Phys. J. C* **81**, 127 (2021), 2011.07140.
- [175] L. A. Escamilla and J. A. Vazquez, Model selection applied to reconstructions of the Dark Energy, *Eur. Phys. J. C* **83**, 251 (2023), 2111.10457.
- [176] E. O. Colgáin, M. M. Sheikh-Jabbari, and L. Yin, Can dark energy be dynamical?, *Phys. Rev. D* **104**, 023510 (2021), 2104.01930.
- [177] M. Raveri, L. Pogosian, M. Martinelli, K. Koyama, A. Silvestri, and G.-B. Zhao, Principal reconstructed modes of dark energy and gravity, *JCAP* **02**, 061, 2107.12990.
- [178] L. Pogosian, M. Raveri, K. Koyama, M. Martinelli, A. Silvestri, G.-B. Zhao, J. Li, S. Peirone, and A. Zucca, Imprints of cosmological tensions in reconstructed gravity, *Nature Astron.* **6**, 1484 (2022), 2107.12992.
- [179] R. C. Bernardo, D. Grandón, J. Said Levi, and V. H. Cárdenas, Parametric and nonparametric methods hint dark energy evolution, *Phys. Dark Univ.* **36**, 101017 (2022), 2111.08289.
- [180] L. A. Escamilla, O. Akarsu, E. Di Valentino, and J. A. Vazquez, Model-independent reconstruction of the interacting dark energy kernel: Binned and Gaussian process, *JCAP* **11**, 051, 2305.16290.
- [181] R. Calderon *et al.* (DESI), DESI 2024: Reconstructing Dark Energy using Crossing Statistics with DESI DR1 BAO data, (2024), 2405.04216.
- [182] M. A. Sabogal, O. Akarsu, A. Bonilla, E. Di Valentino, and R. C. Nunes, Exploring new physics in the late Universe's expansion through non-parametric inference, *Eur. Phys. J. C* **84**, 703 (2024), 2407.04223.
- [183] O. Akarsu, E. O. Colgáin, E. Özüiker, S. Thakur, and L. Yin, Inevitable manifestation of wiggles in the expansion of the late Universe, *Phys. Rev. D* **107**, 123526 (2023), 2207.10609.
- [184] R. Jimenez, L. Verde, T. Treu, and D. Stern, Constraints on the equation of state of dark energy and the Hubble constant from stellar ages and the CMB, *Astrophys. J.* **593**, 622 (2003), astro-ph/0302560.
- [185] J. Simon, L. Verde, and R. Jimenez, Constraints on the redshift dependence of the dark energy potential, *Phys. Rev. D* **71**, 123001 (2005), astro-ph/0412269.
- [186] D. Stern, R. Jimenez, L. Verde, M. Kamionkowski, and S. A. Stanford, Cosmic Chronometers: Constraining the Equation of State of Dark Energy. I:  $H(z)$  Measurements, *JCAP* **02**, 008, 0907.3149.
- [187] M. Moresco, L. Verde, L. Pozzetti, R. Jimenez, and A. Cimatti, New constraints on cosmological parameters and neutrino properties using the expansion rate of the Universe to  $z \sim 1.75$ , *JCAP* **07**, 053, 1201.6658.
- [188] C. Zhang, H. Zhang, S. Yuan, T.-J. Zhang, and Y.-C. Sun, Four new observational  $H(z)$  data from luminous red galaxies in the Sloan Digital Sky Survey data release seven, *Res. Astron. Astrophys.* **14**, 1221 (2014), 1207.4541.
- [189] M. Moresco, Raising the bar: new constraints on the Hubble parameter with cosmic chronometers at  $z \sim 2$ , *Mon. Not. Roy. Astron. Soc.* **450**, L16 (2015), 1503.01116.
- [190] M. Moresco, L. Pozzetti, A. Cimatti, R. Jimenez, C. Maraston, L. Verde, D. Thomas, A. Citro, R. Tojeiro, and D. Wilkinson, A 6% measurement of the Hubble parameter at  $z \sim 0.45$ : direct evidence of the epoch of cosmic re-acceleration, *JCAP* **05**, 014, 1601.01701.
- [191] M. Moresco, <https://gitlab.com/mmoresco/CCcovariance>.
- [192] D. M. Scolnic *et al.* (Pan-STARRS1), The Complete Light-curve Sample of Spectroscopically Confirmed SNe Ia from Pan-STARRS1 and Cosmological Constraints from the Combined Pantheon Sample, *Astrophys. J.* **859**, 101 (2018), 1710.00845.
- [193] Jones *et al.* and Scolnic *et al.*, <https://github.com/PantheonPlusSHOES/DataRelease>.
- [194] A. G. Adame *et al.* (DESI), DESI 2024 VI: Cosmological Constraints from the Measurements of Baryon Acoustic Oscillations, (2024), 2404.03002.
- [195] A. Slosar and J. A. Vazquez, <https://github.com/ja-vazquez/SimpleMC>.
- [196] L. E. Padilla, L. O. Tellez, L. A. Escamilla, and J. A. Vazquez, Cosmological Parameter Inference with Bayesian Statistics, *Universe* **7**, 213 (2021), 1903.11127.
- [197] J. S. Speagle, dynesty: a dynamic nested sampling package for estimating Bayesian posteriors and evidences, *Mon. Not. Roy. Astron. Soc.* **493**, 3132 (2020), 1904.02180.
- [198] R. Trotta, Bayes in the sky: Bayesian inference and model selection in cosmology, *Contemp. Phys.* **49**, 71 (2008), 0803.4089.
- [199] B. Efron, A. Gous, R. Kass, G. Datta, and P. Lahiri, Scales of evidence for model selection: Fisher versus jeffreys, *Lecture Notes-Monograph Series*, 208 (2001).
- [200] D. Rubin *et al.*, Union Through UNITY: Cosmology with 2,000 SNe Using a Unified Bayesian Framework (2023), 2311.12098.
- [201] T. M. C. Abbott *et al.* (DES), The Dark Energy Survey: Cosmology Results With  $\sim 1500$  New High-redshift Type Ia Supernovae Using The Full 5-year Dataset (2024), 2401.02929.
- [202] A. Lewis, GetDist: a Python package for analysing Monte Carlo samples (2019), 1910.13970.
- [203] W. Handley, fgivex: A Python package for functional posterior plotting, *Journal of Open Source Software* **3**, 849 (2018).
- [204] V. Sahni and Y. Shtanov, Brane world models of dark energy, *JCAP* **11**, 014, astro-ph/0202346.
- [205] V. Sahni and Y. Shtanov, Did the Universe loiter at high redshifts?, *Phys. Rev. D* **71**, 084018 (2005), astro-ph/0410221.
- [206] S. Tsujikawa, K. Uddin, S. Mizuno, R. Tavakol, and J. Yokoyama, Constraints on scalar-tensor models of dark energy from observational and local gravity tests, *Phys. Rev. D* **77**, 103009 (2008), 0803.1106.
- [207] S.-Y. Zhou, E. J. Copeland, and P. M. Saffin, Cosmological Constraints on  $f(G)$  Dark Energy Models, *JCAP* **07**, 009, 0903.4610.
- [208] F. Bauer, J. Sola, and H. Stefancic, Dynamically avoiding fine-tuning the cosmological constant: The 'Relaxed Universe', *JCAP* **12**, 029, 1006.3944.
- [209] V. Sahni, A. Shafieloo, and A. A. Starobinsky, Model independent evidence for dark energy evolution from Baryon Acoustic Oscillations, *Astrophys. J. Lett.* **793**, L40 (2014), 1406.2209.

- [210] A. Gomez-Valent, E. Karimkhani, and J. Sola, Background history and cosmic perturbations for a general system of self-conserved dynamical dark energy and matter, *JCAP* **12**, 048, 1509.03298.
- [211] O. Akarsu, J. D. Barrow, C. V. R. Board, N. M. Uzun, and J. A. Vazquez, Screening  $\Lambda$  in a new modified gravity model, *Eur. Phys. J. C* **79**, 846 (2019), 1903.11519.
- [212] O. Akarsu, N. Katirci, N. Özdemir, and J. A. Vázquez, Anisotropic massive Brans-Dicke gravity extension of the standard  $\Lambda$ CDM model, *Eur. Phys. J. C* **80**, 32 (2020), 1903.06679.
- [213] G. Acquaviva, O. Akarsu, N. Katirci, and J. A. Vazquez, Simple-graduated dark energy and spatial curvature, *Phys. Rev. D* **104**, 023505 (2021), 2104.02623.
- [214] E. Özülker, Is the dark energy equation of state parameter singular?, *Phys. Rev. D* **106**, 063509 (2022), 2203.04167.
- [215] Y. L. Bolotin, V. A. Cherkaskiy, O. A. Lemets, D. A. Yerokhin, and L. G. Zazunov, Cosmology In Terms Of The Deceleration Parameter. Part I (2015), 1502.00811.
- [216] S. del Campo, I. Duran, R. Herrera, and D. Pavon, Three thermodynamically-based parameterizations of the deceleration parameter, *Phys. Rev. D* **86**, 083509 (2012), 1209.3415.
- [217] D. M. Naik, N. S. Kavya, L. Sudharani, and V. Venkatesha, Model-independent cosmological insights from three newly reconstructed deceleration parameters with observational data, *Phys. Lett. B* **844**, 138117 (2023).
- [218] H. Epstein, V. Glaser, and A. Jaffe, Nonpositivity of energy density in Quantized field theories, *Nuovo Cim.* **36**, 1016 (1965).
- [219] R. M. Wald and U. Yurtsever, General proof of the averaged null energy condition for a massless scalar field in two-dimensional curved space-time, *Phys. Rev. D* **44**, 403 (1991).
- [220] M. Visser and C. Barcelo, Energy conditions and their cosmological implications, in *3rd International Conference on Particle Physics and the Early Universe* (2000) p. 98, gr-qc/0001099.
- [221] E. Curiel, A Primer on Energy Conditions, *Einstein Stud.* **13**, 43 (2017), 1405.0403.